



Discovery of the Optical Afterglow and Host Galaxy of Short GRB 181123B at $z = 1.754$: Implications for Delay Time Distributions

K. Paterson¹, W. Fong¹, A. Nugent¹, A. Rouco Escorial¹, J. Leja², T. Laskar³, R. Chornock⁴, A. A. Miller^{1,5}, J. Scharwächter⁶, S. B. Cenko^{7,8}, D. Perley⁹, N. R. Tanvir¹⁰, A. Levan^{11,12}, A. Cucchiara^{13,14}, B. E. Cobb¹⁵, K. De¹⁶, E. Berger², G. Terreran¹, K. D. Alexander^{1,6}, M. Nicholl^{17,18}, P. K. Blanchard¹, and D. Cornish¹

¹ Center for Interdisciplinary Exploration and Research in Astrophysics (CIERA) and Department of Physics and Astronomy, Northwestern University, Evanston, IL 60208, USA; kerry.paterson@northwestern.edu

² Center for Astrophysics | Harvard & Smithsonian, 60 Garden Street, Cambridge, MA 02138, USA

³ Department of Physics, University of Bath, Claverton Down, Bath BA2 7AY, UK

⁴ Astrophysical Institute, Department of Physics and Astronomy, 251B Clipping Lab, Ohio University, Athens, OH 45701, USA

⁵ The Adler Planetarium, Chicago, IL 60605, USA

⁶ Gemini Observatory/NSF's NOIRLab, 670 N. A'ohoku Place, Hilo, HI 96720, USA

⁷ Astroparticle Physics Laboratory, NASA Goddard Space Flight Center, Mail Code 661, Greenbelt, MD 20771, USA

⁸ Joint Space-Science Institute, University of Maryland, College Park, MD 20742, USA

⁹ Astrophysics Research Institute, Liverpool John Moores University, 146 Brownlow Hill, Liverpool L3 5RF, UK

¹⁰ School of Physics and Astronomy, University of Leicester, University Road, Leicester LE1 7RH, UK

¹¹ Department of Astrophysics/IMAPP, Radboud University, 6525 AJ Nijmegen, The Netherlands

¹² Department of Physics, University of Warwick, Coventry CV4 7AL, UK

¹³ College of Marin, 120 Kent Ave., Kentfield, CA 94904, USA

¹⁴ University of the Virgin Islands, #2 Brewers Bay Road, Charlotte Amalie, 00802 USVI, USA

¹⁵ Department of Physics, The George Washington University, Washington, DC 20052, USA

¹⁶ Cahill Center for Astrophysics, California Institute of Technology, 1200 E. California Boulevard, Pasadena, CA 91125, USA

¹⁷ Birmingham Institute for Gravitational Wave Astronomy and School of Physics and Astronomy, University of Birmingham, Birmingham B15 2TT, UK

¹⁸ Institute for Astronomy, University of Edinburgh, Royal Observatory, Blackford Hill, Edinburgh EH9 3HJ, UK

Received 2020 May 25; revised 2020 July 7; accepted 2020 July 8; published 2020 July 28

Abstract

We present the discovery of the optical afterglow and host galaxy of the Swift short-duration gamma-ray burst (SGRB) GRB 181123B. Observations with Gemini-North starting ≈ 9.1 hr after the burst reveal a faint optical afterglow with $i \approx 25.1$ mag at an angular offset of $0''.59 \pm 0''.16$ from its host galaxy. Using *grizYJHK* observations, we measure a photometric redshift of the host galaxy of $z = 1.77^{+0.30}_{-0.17}$. From a combination of Gemini and Keck spectroscopy of the host galaxy spanning 4500–18000 Å, we detect a single emission line at 13390 Å, inferred as H β at $z = 1.754 \pm 0.001$ and corroborating the photometric redshift. The host galaxy properties of GRB 181123B are typical of those of other SGRB hosts, with an inferred stellar mass of $\approx 9.1 \times 10^9 M_\odot$, a mass-weighted age of ≈ 0.9 Gyr, and an optical luminosity of $\approx 0.9 L^*$. At $z = 1.754$, GRB 181123B is the most distant secure SGRB with an optical afterglow detection and one of only three at $z > 1.5$. Motivated by a growing number of high- z SGRBs, we explore the effects of a missing $z > 1.5$ SGRB population among the current Swift sample on delay time distribution (DTD) models. We find that lognormal models with mean delay times of ≈ 4 –6 Gyr are consistent with the observed distribution but can be ruled out to 95% confidence, with an additional \approx one to five Swift SGRBs recovered at $z > 1.5$. In contrast, power-law models with $\propto t^{-1}$ are consistent with the redshift distribution and can accommodate up to ≈ 30 SGRBs at these redshifts. Under this model, we predict that $\approx 1/3$ of the current Swift population of SGRBs is at $z > 1$. The future discovery or recovery of existing high- z SGRBs will provide significant discriminating power on their DTDs and thus their formation channels.

Unified Astronomy Thesaurus concepts: Gamma-ray bursts (629)

1. Introduction

Short-duration ($T_{90} < 2$ s) gamma-ray bursts (SGRBs) have long been linked to binary neutron star (BNS) and possibly neutron star–black hole (NS–BH) mergers through indirect observational evidence: the lack of associated supernovae (SNe; Fox et al. 2005; Hjorth et al. 2005a, 2005b; Kocevski et al. 2010; Berger 2014), host galaxy demographics demonstrating a mix of young and old stellar populations (Berger 2009; Leibler & Berger 2010; Fong et al. 2013), low inferred environmental densities (Soderberg et al. 2006; Fong et al. 2015), moderate to large offsets with respect to their host galaxies (Berger 2010; Fong et al. 2010; Church et al. 2011; Fong & Berger 2013; Tunnicliffe et al. 2014), and emission consistent with expectations for r -process kilonovae (Berger

et al. 2013; Tanvir et al. 2013; Tanaka 2016; Metzger 2017; Gompertz et al. 2018; Hotokezaka et al. 2018; Lamb et al. 2019; Troja et al. 2019). The discovery of the BNS merger GW170817 (Abbott et al. 2017a) and the associated SGRB 170817A (Abbott et al. 2017b; Goldstein et al. 2017; Savchenko et al. 2017) provided direct evidence that at least some SGRBs originate from BNS mergers.

As gravitational wave (GW) facilities continue to make ground-breaking discoveries of the first BNS mergers to $z \approx 0.05$ (Abbott et al. 2017a, 2020), SGRBs provide cosmological analogs that can probe the binary merger progenitor population and their rates and evolution to $z \approx 2$. Since 2004, the Neil Gehrels Swift Observatory (Gehrels et al. 2004) has discovered > 130 SGRBs (Lien et al. 2016).

Dedicated campaigns to characterize their host galaxies have led to secure redshift determinations for $\approx 1/3$ of the population, with a peak in the distribution at $z \approx 0.5$ (Fong et al. 2013, 2017; Berger 2014). However, to date, only $\approx 5\%$ of bursts have confirmed redshifts of $z > 1$. This drops to $\approx 1.5\%$ (two events) when considering the confirmed secure SGRBs at $z > 1.5$: GRB 111117A at $z = 2.211$ (Selsing et al. 2018) and GRB 160410A at $z = 1.717$ (Selsing et al. 2016).¹⁹ In general, high-redshift SGRBs are particularly challenging to characterize for a number of reasons. First, a redshift typically requires detection of an optical afterglow for subarcsecond-precision localization and association with a host galaxy, and typical afterglow luminosities scaled to $z > 1$ have faint apparent magnitudes of $r > 24$ mag within hours of burst detection. Second, the sensitivity of Swift is known to fall off at higher redshifts for SGRBs compared to long GRBs due to the different thresholds in the respective detection channels (Guetta & Piran 2005). Third, there are a number of SGRBs with host galaxies that have inferred redshifts of $z > 1.2$ due to their featureless optical spectra (e.g., GRB 051210; Berger et al. 2007) but are too faint to characterize further with current near-infrared (NIR) capabilities. Finally, a broad distribution of delay times (the timescale including the stellar evolutionary and merger timescales) spanning 1 to several Gyr results in an event rate that will peak at low redshifts.

Given the observational challenges, the discovery of additional confirmed SGRBs at $z > 1.5$ may provide significant constraining power on the delay time distribution (DTD). In turn, the DTD inferred from SGRBs can be directly linked to the formation channel of BNS mergers, as primordial binaries versus dynamical assembly within globular clusters will result in different DTDs (Hopman et al. 2006; Belczynski et al. 2018). In the absence of other mechanisms, the merger timescale is determined by the loss of energy and angular momentum due to GWs (Peters 1964), which can be tied to the parameters of the binary (e.g., initial separation, ellipticity; Postnov & Yungelson 2014; Selsing et al. 2018). Many studies have constrained the SGRB DTD by fitting the SGRB redshift distribution, predominantly focused on the $z < 1$ population (Nakar et al. 2006; Berger et al. 2007; Jeong & Lee 2010; Hao & Yuan 2013; Wanderman & Piran 2015; Anand et al. 2018). Other constraints on the DTD have come from studies of the Galactic population of NS binaries (Champion et al. 2004; Beniamini et al. 2016a; Vigna-Gómez et al. 2018; Beniamini & Piran 2019) and SGRB host galaxy demography, as longer delay times will result in an increase in host galaxies with old stellar populations (Zheng & Ramirez-Ruiz 2007; Fong et al. 2013; Behroozi et al. 2014).

Here we present the discovery of the optical afterglow and host galaxy of GRB 181123B at $z = 1.754$, making this event the third confirmed event at $z > 1.5$ and the most distant, secure SGRB with an optical afterglow to date. In Section 2 we describe the discovery and community observations of GRB 181123B. We describe our photometric and spectroscopic observations of GRB 181123B in Section 3. In Sections 4 and 5, we discuss the burst explosion and host galaxy properties, respectively. Our results, including a discussion of GRB 181123B in context with the population of SGRBs and

the implications for the DTD, are given in Section 6. Finally, we summarize our conclusions in Section 7.

Unless otherwise stated, all observations are reported in AB mag and have been corrected for Galactic extinction in the direction of the burst (Schlafly & Finkbeiner 2011). We employ a standard cosmology of $H_0 = 69.6$, $\Omega_M = 0.286$, $\Omega_{\text{vac}} = 0.714$ (Bennett et al. 2014).

2. GRB 181123B

On 2018 November 23 at 05:33:03 UT, the Burst Alert Telescope (BAT; Barthelmy et al. 2005) on board the Neil Gehrels Swift Observatory (Gehrels et al. 2004) discovered and located GRB 181123B at a refined position of R.A., decl. = $12^{\text{h}}17^{\text{m}}27^{\text{s}}.99$, $14^{\circ}35'56''.0$ ($3''.8$ positional uncertainty; 90% confidence) with a duration of $T_{90} = 0.26 \pm 0.04$ s in the 50–300 keV band (90% confidence; Lien et al. 2018). In addition, GRB 181123B showed minimal spectral lag (Norris et al. 2018) and a hardness ratio (between the 50–100 and 25–50 keV bands) of 2.4 (Lien et al. 2016). These properties classify GRB 181123B as a hard-spectrum SGRB. A power-law fit to the data results in a fluence, $f_{\gamma} = (1.2 \pm 0.2) \times 10^{-7}$ erg cm $^{-2}$, in the 15–150 keV band (Evans et al. 2009). Swift’s X-ray Telescope (XRT) began observing the field at $\delta t = 80.25$ s, where δt is the time after the BAT trigger in the observer frame, localizing an uncataloged X-ray source within the BAT region with an enhanced position of R.A., decl. = $12^{\text{h}}17^{\text{m}}28^{\text{s}}.05$, $14^{\circ}35'52''.4$ with a positional uncertainty of $1''.6$ (90% confidence; Goad et al. 2007; Evans et al. 2009; Osborne et al. 2018). Follow-up observations performed by Swift’s Ultraviolet/Optical Telescope (UVOT) resulted in no afterglow detection to a 3σ upper limit of $V > 19.7$ mag at a mid-time of $\delta t = 5148$ s (Oates & Lien 2018).

From the community, the Mobile Astronomical System of Telescope-Robots (MASTER; Lipunov et al. 2010) obtained optical follow-up observations at $\delta t = 2.7$ and 20.2 hr and did not detect any source in or around the XRT position to upper limits of $\gtrsim 17$ and $\gtrsim 18.1$ mag, respectively (Lipunov et al. 2018). In addition, radio observations with the Australia Telescope Compact Array (ATCA; Frater et al. 1992) were conducted at $\delta t = 12.5$ hr; no radio emission was detected to 3σ upper limits of 66 and 69 μJy at 5 and 9 GHz, respectively (Anderson et al. 2018).

3. Observations

3.1. Afterglow Observations

3.1.1. Gemini Optical Discovery

We initiated *i*-band target-of-opportunity (ToO) observations of the field of GRB 181123B with the Gemini Multi-Object Spectrograph (GMOS; Crampton et al. 2000), mounted on the 8 m Gemini-North telescope (PI: Fong; Program GN-2018B-Q-117), at a mid-time of 2018 November 23.618 UT or $\delta t = 9.2$ hr (Fong et al. 2018). We obtained 18×90 s of exposures, resulting in a total of 1620 s on source, at an airmass of 1.7 and average seeing of $1''.0$. We used a custom pipeline,²⁰ using routines from *ccdproc* (Craig et al. 2017) and *astropy* (Astropy Collaboration et al. 2013; Price-Whelan et al. 2018) to perform bias-subtraction, flat-fielding, and gain-correction calibrations. We aligned and coadded the data and

¹⁹ In the sample of secure SGRBs, we include events with $T_{90} < 2$ s but exclude cases like GRB 090426A, an SGRB with γ -ray and environmental properties that otherwise are more consistent with a massive star progenitor (Antonelli et al. 2009; Levesque et al. 2010).

²⁰ https://github.com/KerryPaterson/Imaging_pipelines/GMOS_pipeline.py

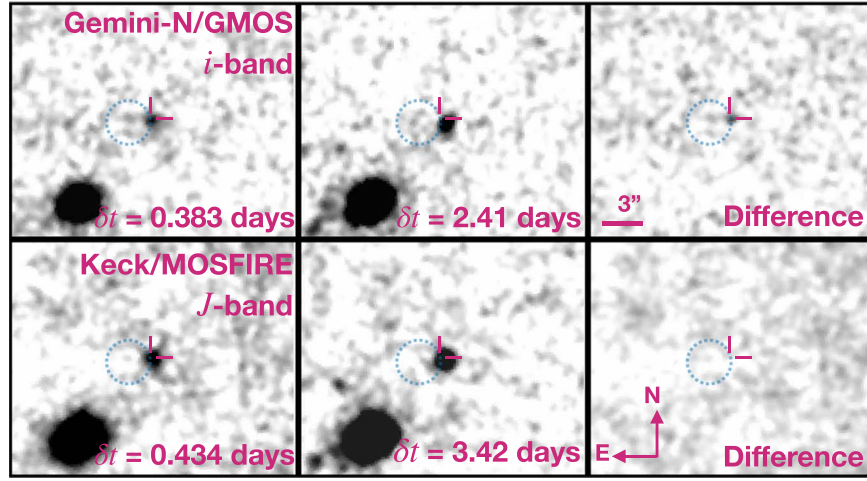


Figure 1. First (left) and second (middle) epochs of *i*- and *J*-band observations and the difference between the two images produced using HOTPANTS (right), smoothed for display purposes. The circle shows the 90% XRT localization of GRB 181123B. The *i*-band difference image reveals a faint, $i = 25.10 \pm 0.39$ mag source on the edge of the XRT position, whose position is marked by the crosshair, which we consider to be the optical afterglow. We find no source in the *J*-band difference image to a limit of $J \gtrsim 23.2$ mag.

Table 1
Afterglow and Host Galaxy Observations of GRB 181123B

| Date ^a (UT) | δt^a (days) | Filter | Telescope | Instrument | Total Exp. Time (s) | Afterglow (AB mag) | Host (AB mag) | A_λ^b (AB mag) |
|---------------------------|------------------------|--------------|-----------|-------------|------------------------|-----------------------|------------------|---------------------------|
| Imaging | | | | | | | | |
| 2018 Nov 23.618 | 0.38 | <i>i</i> | Gemini-N | GMOS | 1620 | 25.10 ± 0.39 | ... | 0.06 |
| 2018 Nov 23.669 | 0.43 | <i>J</i> | Keck I | MOSFIRE | 2880.5 | >23.2 | 23.05 ± 0.32 | 0.03 |
| 2018 Nov 25.637 | 2.40 | <i>i</i> | Gemini-N | GMOS | 2400 | ... | 23.79 ± 0.19 | 0.06 |
| 2018 Nov 25.496 | 2.27 | <i>J</i> | MMT | MMIRS | 3717.7 | >23.3 | 22.65 ± 0.26 | 0.03 |
| 2018 Nov 26.655 | 3.42 | <i>J</i> | Keck I | MOSFIRE | 2138.5 | ... | 22.85 ± 0.23 | 0.03 |
| 2019 Jan 17.545 | 55.31 | <i>K</i> | MMT | MMIRS | 1704 | ... | 22.33 ± 0.23 | 0.01 |
| 2019 Jan 20.464 | 58.23 | <i>K</i> | MMT | MMIRS | 1394.2 | ... | 22.39 ± 0.41 | 0.01 |
| 2019 Feb 3.312 | 72.08 | <i>r</i> | Gemini-S | GMOS | 1800 | ... | 23.84 ± 0.19 | 0.08 |
| 2019 Feb 3.340 | 72.11 | <i>g</i> | Gemini-S | GMOS | 1800 | ... | 24.08 ± 0.23 | 0.12 |
| 2019 Feb 3.370 | 72.14 | <i>z</i> | Gemini-S | GMOS | 1800 | ... | 23.84 ± 0.22 | 0.04 |
| 2019 May 24.275 | 182.04 | <i>H</i> | MMT | MMIRS | 2987.4 | ... | 22.61 ± 0.19 | 0.02 |
| 2020 Mar 5.329 | 468.10 | <i>Y</i> | MMT | MMIRS | 3584.9 | ... | 22.78 ± 0.24 | 0.03 |
| Spectroscopy | | | | | | | | |
| 2019 Feb 26.495 | 95.26 | <i>GG455</i> | Keck II | DEIMOS | 5400 | | | |
| 2019 Apr 10.678 | 137.95 | <i>JH</i> | Gemini-S | FLAMINGOS-2 | 3600 | | | |

Notes. All magnitudes are in the AB system, and uncertainties correspond to 1σ .

^a Based on mid-time of observation.

^b Galactic extinction in the direction of the burst (Schlafly & Finkbeiner 2011).

performed astrometry relative to Gaia DR2 (Gaia Collaboration et al. 2016, 2018; Lindegren et al. 2018).

We obtained a second, deeper set of *i*-band Gemini-N/GMOS observations at a mid-time of 2018 November 25.637 UT ($\delta t = 2.41$ days) with significantly improved image quality compared to the first set (airmass of 1.3, seeing of $0''.7$). We detect an extended source in the epoch 2 observations near the XRT position, presumed to be the host galaxy (see Section 3.2). To assess any fading between epochs 1 and 2, we align the epoch 2 observations with respect to epoch 1 and perform image subtraction using HOTPANTS (Becker 2015; Figure 1) between the two epochs. A source is found within the enhanced XRT position in the difference image, which we consider to be the optical afterglow. Performing aperture photometry with standard IRAF (Tody 1986) packages directly on the residual image and photometrically calibrating to the Sloan Digital Sky Survey (Fukugita et al. 1996; Gunn et al.

2006; Eisenstein et al. 2011; Ahn et al. 2012), we measure an afterglow brightness of $i = 25.10 \pm 0.39$ mag at $\delta t = 9.2$ hr. Calibrated to Gaia DR2, we determine a position at R.A., decl. = $12^h17^m27^s.94$, $14^\circ35'52''.66$ with a positional uncertainty of $0''.10$ accounting for the afterglow centroid and astrometric uncertainties. A summary of our observations and aperture photometry is given in Table 1.

3.1.2. NIR Photometric Observations

We obtained *J*-band observations of GRB 181123B with the Multi-Object Spectrometer For Infra-Red Exploration (MOSFIRE; McLean et al. 2012), mounted on the 10 m Keck I telescope (PI: Miller; Program 2018B_NW254), at a mid-time of 2018 November 23.669 UT or $\delta t = 10.4$ hr (first reported in Paterson & Fong 2018). We obtained a total of 2880.5 s on source from 36×58 and 27×29 s exposures in cloudy

conditions with 1'' seeing. We developed and used a custom MOSFIRE pipeline²¹ (using routines from `ccdproc` and `astropy`) to reduce the data in a similar manner to Gemini but with an additional sky-subtraction routine to take into account the varying IR sky. We aligned and coadded the data, dividing first by the exposure time to ensure equal weights, and performed astrometry relative to Gaia DR2.

We detect an extended source near the XRT position and initiated a second set of observations with Keck (Paterson et al. 2018) through a ToO program (PI: Fong; Program 2018B_NW249) at a mid-time of 2018 November 26.655 UT or $\delta t = 3.42$ days. We obtained 40×58 s exposures, for a total of 2138.5 s on source, in clear conditions with seeing of 0''.9. The clear conditions and improved seeing of these observations provided a deeper image, allowing us to use it as a template for image subtraction. We align this image with the epoch 1 observations and perform image subtraction using HOTPANTS. We do not detect any residuals at the position of the afterglow to a 3σ limit of $J \gtrsim 23.2$ mag, calibrated to the Two Micron All Sky Survey (2MASS; Skrutskie et al. 2006) and converted to the AB system. The images are shown in Figure 1.

We also obtained J -band observations with the Magellan Infrared Spectrograph (MMIRS; McLeod et al. 2012), mounted on the 6.5 m MMT telescope (PI: Fong; Program 2018C-UAO-G4), at $\delta t = 2.27$ days. We developed and used a custom MMIRS pipeline²² to reduce data in a similar manner to MOSFIRE. We perform image subtraction relative to the second epoch of Keck and do not detect any residuals at the position of the afterglow to a 3σ limit of $J \gtrsim 23.3$ mag, calibrated to 2MASS and converted to the AB system. We note that the lack of afterglow detection in the J -band is consistent with the steady brightness of the host galaxy over all three epochs (Table 1).

3.2. Host Observations

3.2.1. Host Galaxy Assignment

We quantify the probability that the coincident extended source is the host galaxy of GRB 181123B. Based on the XRT position alone, we calculate the probability of the chance coincidence (P_{cc} ; Bloom et al. 2002) of the GRB with the galaxy to be $P_{cc} = 0.012$. From Gemini i -band imaging, we measure an afterglow brightness of $i = 23.85 \pm 0.19$ mag and determine a position of R.A., decl. = $12^h17^m27^s.91$, $14^\circ35'52''27$ with a positional uncertainty of 0''.07. Relative to the optical afterglow position, we calculate an offset of $0''.59 \pm 0''.16$, taking into account the afterglow and host centroids and relative astrometric uncertainty. Using the optical afterglow, we calculate $P_{cc} = 4.4 \times 10^{-3}$. Calculating a P_{cc} for nearby extended sources in the field, the next most probable host has $P_{cc} = 0.07$, while all other sources have values close to unity. Thus, we conclude that the extended source is the host galaxy of GRB 181123B.

3.2.2. Multiband Imaging

We obtained late-time g -, r -, and z -band observations with Gemini-South/GMOS at $\delta t \approx 72$ days (PI: Fong; Program GS-2018B-Q-112). We also obtained YHK observations, where the Y -band observations are calibrated to UKIRT (Hewett et al. 2006; Lawrence et al. 2007; Hodgkin et al. 2009) and converted to the AB system, with MMT/MMIRS (PI: Fong; Programs 2019A-UAO-G7 and 2020A-UAO-G212-20A) with $\delta t > 50$ days.

The details of these observations are summarized in Table 1. A color composite image of the field made from the g , r , i , z , J , and K filters, along with the photometry of the host galaxy from all bands, is shown in Figure 2.

3.2.3. Keck Optical Spectroscopy

We obtained an optical spectrum of the host of GRB 181123B with the DEep Imaging Multi-Object Spectrograph (DEIMOS; Faber et al. 2003), mounted on Keck I (PI: Paterson; Program 2019A_O329). We obtained 3×1800 s exposures in clear conditions with 0''.9 seeing. Using the 600ZD grating, a GG455 order-block filter, and a central wavelength of 7498 Å, the spectrum roughly covers the wavelength range 4400–9600 Å with a central resolving power, $R = 2142$. We used standard IRAF routines in the `ctioslit` package to reduce and coadd the data. We performed wavelength calibrations using an NeArKrXe arc taken just before the observations and used the standard star Feige 34 for spectrophotometric calibration. We extracted the error spectrum and normalized by $1/\sqrt{N}$, where N is the number of images used in the coadd. The resulting spectrum, scaled to the multiband photometry, is shown in Figure 3.

The spectrum is featureless, with no lines above a signal-to-noise ratio (S/N) > 5 . There is a faint continuum but no clear features. In particular, the lack of identifiable lines or features suggests that the host galaxy is at $z > 1.4$.

3.2.4. Gemini NIR Spectroscopy

We obtained NIR spectroscopy with the Facility Near-Infrared Wide-field Imager and Multi-Object Spectrograph for Gemini (FLAMINGOS-2; Eikenberry et al. 2004), mounted on the 8 m Gemini-South telescope, using a fast-turnaround program (PI: Paterson; Program GS-2019A-FT-107). Using a JH/JH grism/filter setup with a central wavelength of 13900 Å, we obtained 30×120 s exposures for a total of 3600 s on source, roughly covering the wavelength range 9800–18000 Å and with a central $R = 1177$. We used standard procedures from the `gemini` package within IRAF to reduce and coadd the data. We performed wavelength calibration using Ar arc lamp spectra and flux calibration and telluric line corrections with the standard star HIP 56736 using the generalized IDL routine `xtellcor_general` (Vacca et al. 2003) from the `Spextool` package (Cushing et al. 2004). We extracted the error spectrum in the same manner as the Keck spectrum; the FLAMINGOS-2 spectrum, scaled to the YJH photometry, is shown in Figure 3.

3.2.5. Redshift Determination

We identify a single emission line in the FLAMINGOS-2 spectrum with an $S/N = 13.5$ at 13390.0 Å. No other line features are present with $S/N \gtrsim 5$. Given that this is the only

²¹ https://github.com/KerryPaterson/Imaging_pipelines/MOSFIRE_pipeline.py

²² https://github.com/KerryPaterson/Imaging_pipelines/MMIRS_pipeline.py

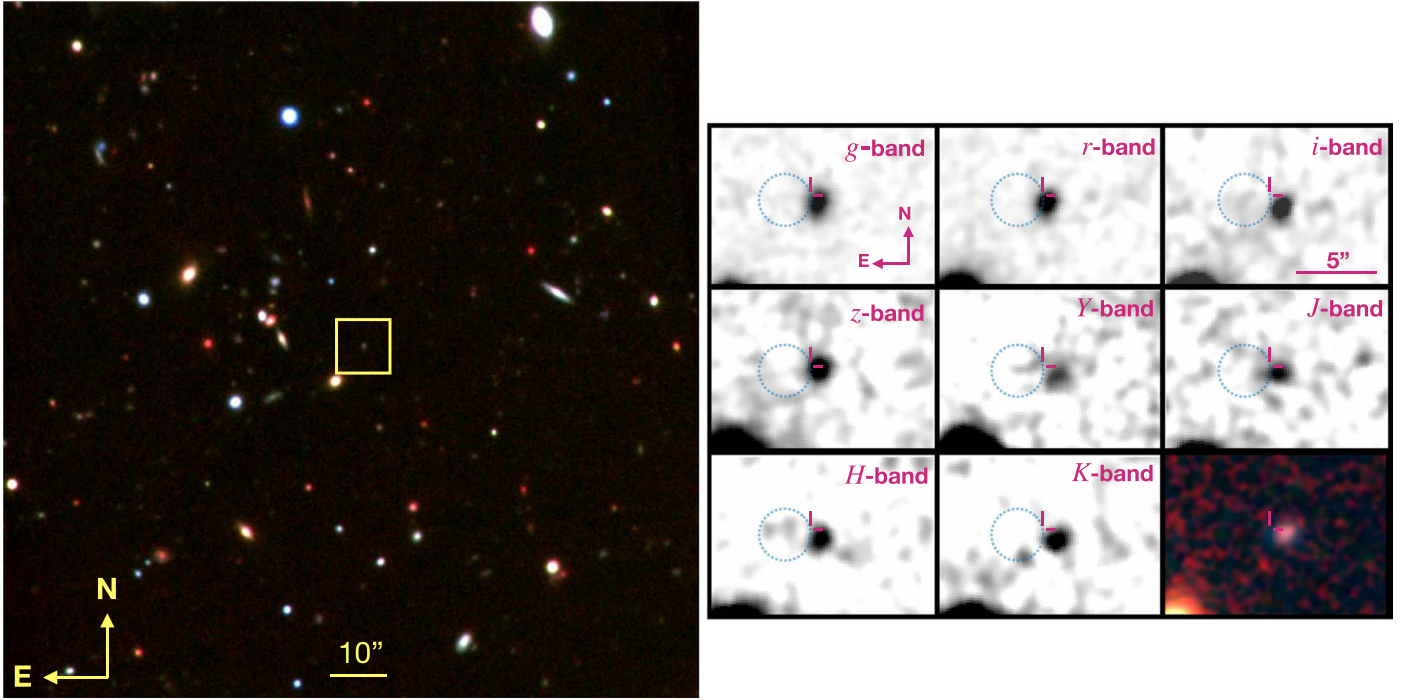


Figure 2. Left: color composite six-filter image of GRB 181123B observations created using *AstroImageJ* (Collins et al. 2017; g = blue, r = cyan, i = green, z = yellow, J = red, K = magenta) showing the large field of view. Right: multiband photometry of GRB 181123B’s host galaxy (zoomed region highlighted by the yellow box of the color composite image) obtained with the MMT, Gemini, and Keck. The last panel is the color composite image. The Swift/XRT position is denoted by the blue circle (90% confidence), and the images are smoothed for display purposes.

clear line in the spectrum, we explore whether the line can be matched to one of four possibilities based on the predominant features in star-forming (SF) galaxy spectra ([O II] $\lambda 3727$, H β $\lambda 4861$, [O III] $\lambda 4959/\lambda 5007$, or H α $\lambda 6563$) given the photometric redshift of photo- $z = 1.77^{+0.30}_{-0.17}$ based on the eight-filter host photometry (discussed in Section 3.2.2) and the absence of any other features over 4400–18000 Å.

If this line is H α , the H β and [O II] lines would fall in regions of low error and should have been detected. Similarly, if this line is either of the [O III] $\lambda 4959/\lambda 5007$ doublet, the H β and [O II] lines should have been detected. In this case, the resulting redshifts would be $z = 1.70$ and 1.67 , respectively. If the line is [O II], the resulting redshift of $z = 2.59$ is not consistent with the photo- z (see Section 5), and the H β line should have been detected. Finally, if the line is H β , the resulting redshift is fully consistent with the photo- z . The location of the [O III] doublet is in a region of strong telluric absorption, the location of [O II] is in a region of high noise, and the location of H α is not covered. Considering that the [O II] line is not detected due to the high noise, we calculate an [O II]/H β ratio based on an S/N of 5 for the [O II] line and assuming a similar line width, on the order of $\lesssim 5$. We thus determine that the most likely candidate for this line is H β , which would place GRB 181123B at $z = 1.754 \pm 0.001$. We thus use this redshift for our subsequent analysis.

4. Afterglow Properties

Adopting the standard synchrotron model for a relativistic blast wave expanding into a constant density medium (Sari et al. 1998; Granot & Sari 2002), we use the broadband afterglow observations to infer physical parameters, such as the electron power-law index (p), isotropic-equivalent kinetic energy ($E_{K,iso}$), circumburst density (n), and fraction of

electrons in the electric (ϵ_e) and magnetic field (ϵ_B) using the standard relations from Granot & Sari (2002). The relation of the observed flux to the physical parameters requires knowledge of the location of the spectral break frequencies with respect to the observing bands, and hence the part of the spectrum each band falls on.

For the X-rays, we download the Swift/XRT data available from the Swift website (Evans et al. 2009). We make use of the late-time observations for our fits due to excess flux at early times. We use the temporal and spectral power-law indices from the X-rays (α_X and β_X , respectively), to determine if the X-ray band falls below or above the cooling frequency, ν_c , through the calculation of p . Fitting a power law to the XRT light curve at $\delta t > 700$ s using χ^2 -minimization, we obtain $\alpha_X = -0.96^{+0.13}_{-0.11}$. We use XSPEC (Arnaud 1996) to fit a two-absorption power law to the XRT spectrum over $\delta t = 561$ –16,171 s. Fixing the Galactic hydrogen column density, $N_{H,Gal} = 3.08 \times 10^{20} \text{ cm}^{-2}$ (Willingale et al. 2013), and $z = 1.754$, we find an intrinsic hydrogen column density of $N_{H,int} = 8.40^{+61.10}_{-8.40} \times 10^{20} \text{ cm}^{-2}$ and photon index $\Gamma_X = 2.392^{+0.133}_{-0.422}$. We determine $\beta_X = -1.39^{+0.13}_{-0.42}$ from the definition $\beta_X \equiv 1 - \Gamma_X$. Using the median values for the spectral parameters, we calculate an unabsorbed X-ray flux at 2.3 hr of $F_X = 2.07 \pm 0.43 \text{ erg s}^{-1} \text{ cm}^{-2}$ (0.3–10 keV) or $F_{\nu,X} = 0.13 \mu\text{Jy}$ at 1.7 keV.

We calculate the value of p from both indices for two scenarios: $\nu_m < \nu_X < \nu_c$, where ν_m is the peak frequency of the synchrotron spectrum, and $\nu_X > \nu_c$, requiring the value of p to be in agreement for each scenario. We find that $\nu_X > \nu_c$, with a weighted mean and 1σ uncertainty of $\langle p \rangle = 2.01 \pm 0.15$. Since typical values of p range between 2 and 3 due to implications that arise from the distribution of the Lorentz

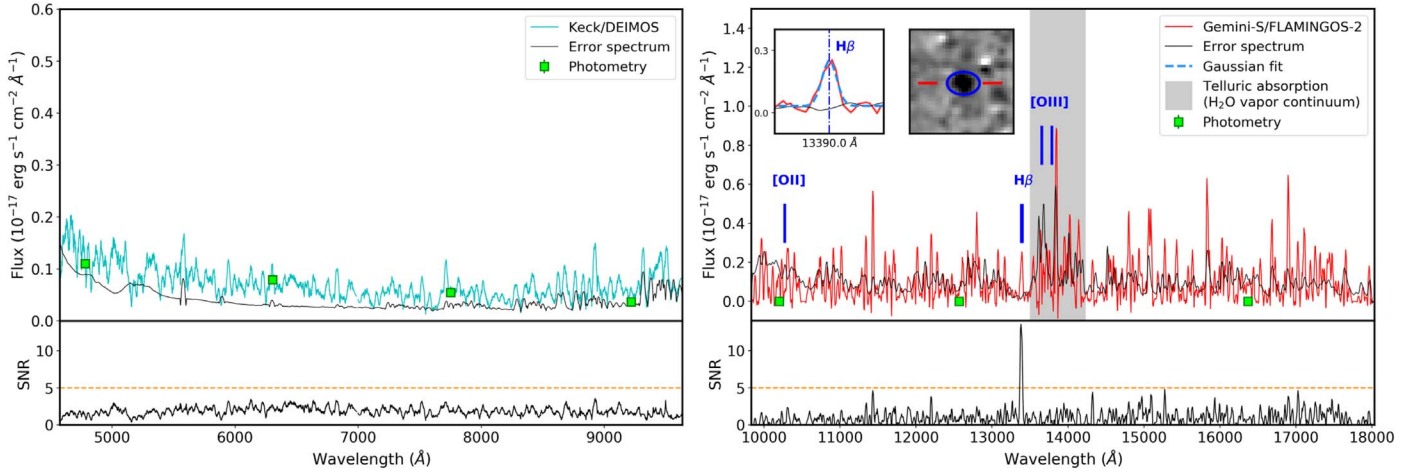


Figure 3. Top panels: optical (left) and NIR (right) spectra of GRB 181123B’s host galaxy. The cyan line shows the optical spectrum from Keck/DEIMOS. The red line shows the NIR spectrum from Gemini-S/FLAMINGOS-2. The black lines show the error spectra. The gray band shows the region of strong telluric absorption caused by continuum water vapor absorption. The spectrum has been scaled to the photometry (green squares) and smoothed using a 75-windowed, second-order polynomial Savitzky–Golay filter (Savitzky & Golay 1964). The spectrum and photometry are dereddened by the Galactic extinction in the direction of the burst (Cardelli et al. 1989; Schlafly & Finkbeiner 2011). The blue lines correspond to the positions of strong emission lines expected at $z = 1.754$; the [O II] and [O III] doublets are both in regions of large error. The insets in the right panel show a zoomed-in view of the position of the $H\beta$ line for the 1D spectrum fitted with a Gaussian (left inset) and the 2D spectrum highlighting the emission line (right inset). Bottom panels: S/N of the respective spectra. The orange dashed line corresponds to $S/N = 5$. Only a single line with $S/N = 13.5$ is seen in the NIR at 13390 \AA , which we identify as $H\beta$.

factors (e.g., de Jager & Harding 1992), we employ $p = 2.1$ in subsequent analysis.

Since the X-rays lie above ν_c , the isotropic-equivalent kinetic energy does not depend on the circumburst density and thus can be used to constrain $E_{K,iso}$ directly, assuming fixed values for ϵ_e and ϵ_B . Fixing $z = 1.754$, $D_L = 13,457 \text{ Mpc}$, $\nu_X = 1.7 \text{ keV}$ (the logarithmic center of the 0.3–10 keV XRT band), and $\epsilon_e = \epsilon_B = 0.1$ (see Zhang et al. 2015), we use $F_{\nu,X} = 0.13 \mu\text{Jy}$ at 0.10 days to calculate

$$E_{K,iso,52} = 0.14 \pm 0.03, \quad (1)$$

where $E_{K,iso,52}$ is $E_{K,iso}$ in units of 10^{52} erg . An additional constraint can be set in the limiting case that ν_c is at the lower edge of the X-ray band, $\nu_{c,max} = 0.3 \text{ keV}$, which places a lower limit on the combination of $E_{K,iso}$ and n of

$$n^2 E_{K,iso,52} > 5.99 \times 10^{-5}, \quad (2)$$

where n is in units of cm^{-3} . For the optical and NIR bands, we assume that $\nu_m < \nu_{opt/NIR} < \nu_c$. From $i = 25.10 \pm 0.39$ at 0.38 days, we calculate $F_{\nu,opt} = 0.33 \pm 0.14 \mu\text{Jy}$, and obtain

$$n^{0.4} E_{K,iso,52} = 0.03 \pm 0.01, \quad (3)$$

and the NIR constraint of $F_{\nu,NIR} < 1.87 \mu\text{Jy}$ at 0.43 days, gives us

$$n^{0.4} E_{K,iso,52} < 0.32. \quad (4)$$

Finally, we use the available 9 GHz ATCA upper limit at 0.52 days (Anderson et al. 2018) and make the assumption $\nu_{sa} < \nu_{radio} < \nu_m$, where ν_{sa} is the self-absorption frequency, to calculate

$$n^{0.6} E_{K,iso,52} < 0.2. \quad (5)$$

For the case where $\nu_{radio} < \nu_{sa}$, we find no difference in the cumulative allowed parameter space, which is primarily determined by the optical and X-ray detections and the cooling frequency constraint.

The allowed $E_{K,iso}$ – n parameter space for GRB 181123B, calculated from combining the probability distributions from the above relations, is shown in Figure 4. We calculate the medians for the parameters, $E_{K,iso,52} = 0.13^{+0.02}_{-0.02} \text{ erg}$ and $n = 0.04^{+0.02}_{-0.01} \text{ cm}^{-3}$, from the 1D probability distributions.²³ We also calculate the above constraints for $\epsilon_B = 0.01$, finding $E_{K,iso,52} = 0.14^{+0.02}_{-0.02} \text{ erg}$ and $n = 1.10^{+0.87}_{-0.32} \text{ cm}^{-3}$ (Figure 4). Motivated by the low value of $\epsilon_B \approx 10^{-4}$ – 10^{-2} derived for GW170817’s afterglow (e.g., Wu & MacFadyen 2018; Hajela et al. 2019), as well as those derived for Swift SGRBs (Santana et al. 2014; Zhang et al. 2015), we explore the possibility of a low value of ϵ_B and find that the allowed parameter space is completely ruled out for $\epsilon_B \lesssim 10^{-3}$ (for $\epsilon_e = 0.1$). In summary, we derive $E_{K,iso} \approx 0.13$ – $0.14 \times 10^{52} \text{ erg}$ and $n \approx 0.04$ – 1.10 cm^{-3} for GRB 181123B. Using the value of $E_{K,iso}$ and $E_{\gamma,iso} = 5.0 \times 10^{51} \text{ erg}$,²⁴ we also calculate a gamma-ray efficiency of 0.78, just above the median of 0.57 found by Fong et al. (2015) and in line with the higher values found by Beniamini et al. (2016b) when no synchrotron self-Compton component is included.

5. Host Galaxy Properties

To characterize the host galaxy of GRB 181123B, we use Prospector (Johnson & Leja 2017; Leja et al. 2017), a stellar population modeling code that employs a library of flexible stellar population synthesis (FSPS) models (Conroy et al. 2009; Conroy & Gunn 2010) and determines the best-fit solution and posterior parameter distributions with Dynesty (Speagle 2020) through a nested sampling algorithm

²³ For these parameters, we find a global Compton $Y \approx 0.1$ (Sari & Esin 2001), suggesting that inverse-Compton (IC) cooling is not significant. Where IC cooling becomes more important for lower values of ϵ_B , in practice, the inclusion of Klein–Nishina corrections severely limits the maximum Compton Y -parameter for faint bursts, especially at low density (Nakar et al. 2009). Thus, we do not include IC cooling in our analysis.

²⁴ We note that because we do not model the gamma-ray spectrum in this work, we do not know the true bolometric correction but have used a fiducial value of 5.

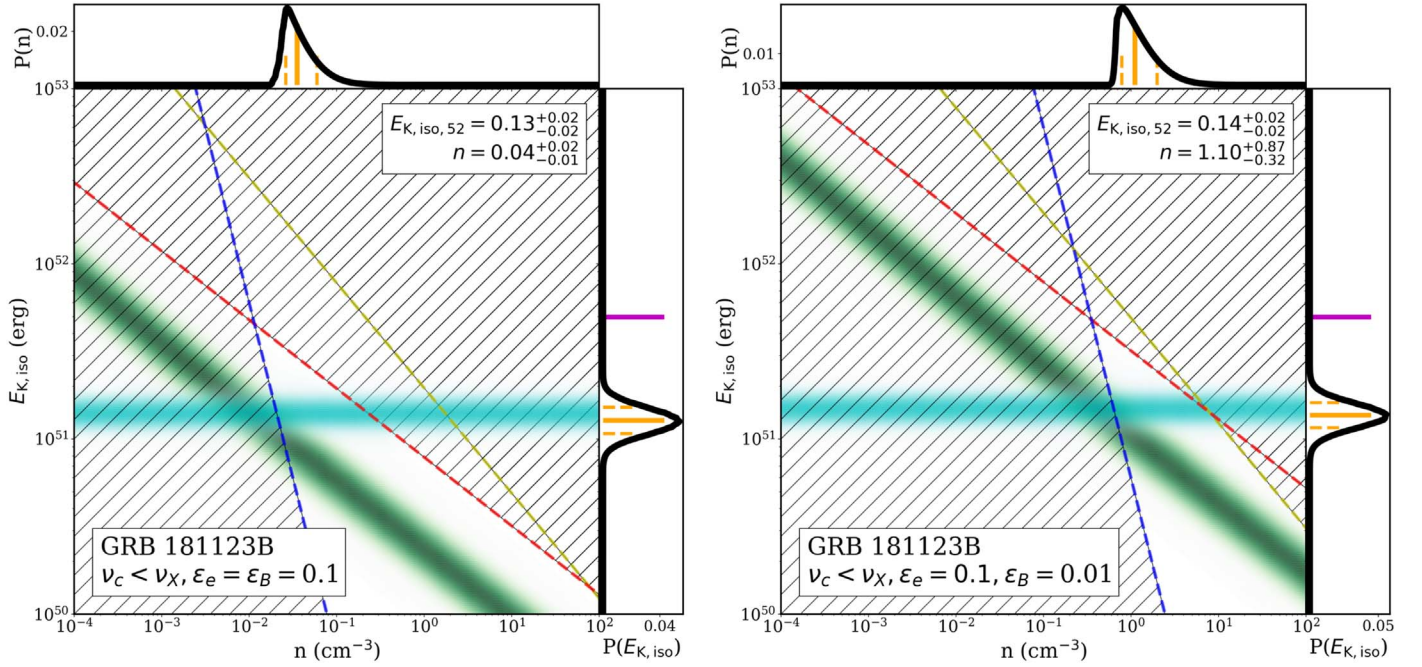


Figure 4. Isotropic-equivalent kinetic energy, $E_{K,iso}$, vs. circumburst density, n , for the afterglow of GRB 181123B. The cyan and green bands show the solution from the X-ray and optical detections, respectively, where the width corresponds to 1σ confidence. The fading in color represents the drop-off in probability going away from the center of each constraint. The red, yellow, and blue lines correspond to the solutions from limits set by the NIR band, radio band, and cooling frequency, respectively, where the corresponding hatched regions illustrate the parameter space ruled out by the limits. The solid black distributions to the top and right of the parameter space show the 1D probability of $E_{K,iso}$ and n , respectively. The solid magenta line to the right shows $E_{\gamma,iso}$. Left: case where $\epsilon_B = 0.1$. Right: case where $\epsilon_B = 0.01$.

(Skilling 2004, 2006). We fit our photometric data to independently determine the redshift, z_{photo} , as well as the following stellar population properties: rest-frame attenuation in mags (A_V), stellar metallicity (Z), mass (M_* in units of solar mass), star formation history (SFH), and age of the galaxy at the time of observation (t_{age}). During fits, these parameters can either be set free to determine the posterior distribution or fixed to a specific value and adopt priors that are uniform across the allowed parameter space within FSPS. For the SFH, we employ a parametric delayed- τ model, such that $SFR(t) \propto te^{-t/\tau}$, with τ as an additional free parameter. We then use t_{age} and τ to convert to a mass-weighted age of the galaxy, t_{gal} , by $t_{gal} = t_{age} - \frac{\int_0^{t_{age}} SFR(t) dt}{\int_0^{t_{age}} SFR(t) dt}$. We use a Chabrier initial mass function (Chabrier 2003) and a Milky Way extinction law ($R = 3.1/E(B - V)$; Cardelli et al. 1989), turn nebular emission on to model an SF galaxy, and add additional attenuation toward the nebular regions to account for the fact that stars in SF regions will generally experience twice the attenuation of normal stars (Calzetti et al. 2000; Price et al. 2014).

First, we perform a fit to determine the photometric redshift, z_{photo} , using the *grizYJHK* photometry and 1σ uncertainties of GRB 181123B's host galaxy, along with the relevant transmission curves for each filter (obtained from the corresponding website of each instrument;^{25,26,27} Crampton et al. 2000; McLean et al. 2012; McLeod et al. 2012). We allow a range of $z = 0.2-4$ and Z , A_V , τ , t_{age} , and M_* to be additional free parameters. We find a single-peaked posterior distribution for

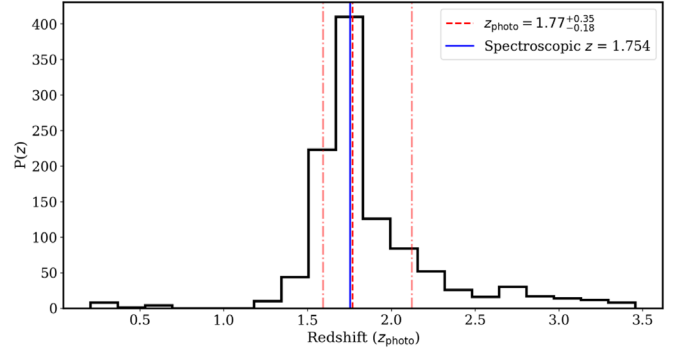


Figure 5. Posterior distribution of the redshift, z_{photo} , found by Prospector using the photometric data of GRB 181123B's host galaxy over the final 1085 iterations. We find a single peak of $z_{photo} = 1.77^{+0.30}_{-0.17}$, fully consistent with the spectroscopically determined redshift, assuming the single emission line is $H\beta$.

the redshift using the final 1085 iterations of the sampling once the solution has converged (Figure 5), with $z_{photo} = 1.77^{+0.30}_{-0.17}$. This is consistent with the redshift determined from the single emission line identified in the NIR spectrum if the line is $H\beta$. There is a low-probability tail (<0.1) extending to high redshifts, but solutions beyond $z \approx 2.5$ are inconsistent with the spectrum and photometric colors.

Next, we fix the redshift to the spectroscopically determined value of $z = 1.754$, set the maximum value of t_{age} to be the age of the universe at that redshift (3.755 Gyr), and fit for the remaining stellar population properties. To self-consistently account for attenuation while calculating the SFR, we also include an additional synthetic photometric data point calculated from the spectrum by defining a box filter of 300 Å width centered on the $H\beta$ emission line. We find final values of $\log(Z/Z_{\odot}) = -0.57^{+0.36}_{-0.49}$, $A_V = 0.23^{+0.4}_{-0.10}$ mag, \log

²⁵ <https://www2.keck.hawaii.edu/inst/mosfire/throughput.html>

²⁶ <https://www.cfa.harvard.edu/mmti/mmirs/instrstats.html>

²⁷ <https://www.gemini.edu/instrumentation/gmos/components#Filters>

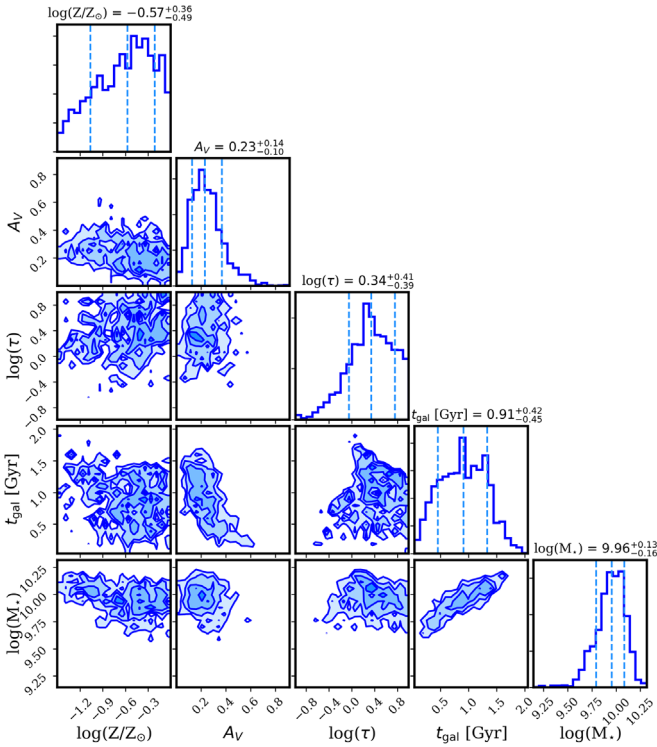


Figure 6. Corner plots showing the fitted parameters found by *Prospector* using the photometric data of GRB 181123B’s host galaxy using the spectroscopic $z = 1.754$.

$(\tau) = 0.34^{+0.41}_{-0.39}$ Gyr, and $\log(M_*) = 9.96^{+0.13}_{-0.16} M_\odot$. Calculating the mass-weighted age from the SFH gives $t_{\text{gal}} = 0.91^{+0.42}_{-0.45}$ Gyr. The corner plot produced by *Prospector*, showing the parameter posterior distributions, is shown in Figure 6, while the observed photometry (including the synthetic photometric point around $H\beta$), overplotted with the model spectrum and photometry, as well as the observed spectrum, is shown in Figure 7. We note that there are well-known degeneracies between A_V , Z , and t_{age} (Conroy 2013). We explore these degeneracies by fixing metallicity and rest-frame attenuation to a range of values to see how they affect the parameter solutions. Except when A_V is set to the extreme cases of 0 or 1 mag, which produce an unconstrained t_{age} and a poor fit to the data, respectively, the remaining parameter solutions remain within a narrow range of values.

Scaling by the total mass formed, we find $\text{SFR} = 10.31^{+5.42}_{-2.83} M_\odot \text{ yr}^{-1}$ and $\log(\text{sSFR}) = -8.95^{+0.26}_{-0.28} \text{ yr}^{-1}$ from the spectral energy distribution (SED). In principle, we can also use the NIR emission line to determine an SFR by calculating an $H\alpha$ flux using relations from Kennicutt (1998). This method, however, is subject to stellar absorption and dust attenuation and relies on typical $H\beta/H\alpha$ line ratios, which can lead to deviation from the true SFR by several factors (Moustakas et al. 2006). Indeed, without correction, we determine $\text{SFR}_{H\beta} = 4.91 \pm 0.43 M_\odot \text{ yr}^{-1}$, ~ 2 times lower than the SED SFR. We therefore consider the SFR calculated from the SED to be a true representation of the SFR.

6. Discussion

6.1. Comparing GRB 181123B to the SGRB Population

At $z = 1.754$, GRB 181123B is among the most distant SGRBs with a confirmed redshift to date. Comparing the γ -ray

T_{90} , hardness ratio, and fluence to those of Swift SGRBs across $z = 0.1$ – 2.2 (Lien et al. 2016), GRB 181123B lies near the median value compared to the rest of the population, solidifying its membership in this class. The SGRB GRB 111117A originates from a host galaxy at a higher redshift of $z = 2.211$ and also has similar γ -ray properties to those of other SGRBs (Selsing et al. 2018). In contrast, the high-redshift GRB 090426A at $z = 2.609$ has a measured $T_{90} \sim 1.3$ s, which would ostensibly place it in the SGRB class, but it has spectral and energy properties that are otherwise more similar to those of long GRBs (Antonelli et al. 2009; Levesque et al. 2010), so the classification and progenitor of this burst are unclear and we do not include it in our discussion of secure SGRBs. Due to its featureless optical host galaxy spectrum (Berger et al. 2007), GRB 051210 is likely at $z > 1.4$ but does not have a secure redshift. Finally, GRB 160410A has an afterglow redshift of $z = 1.717$ (Selsing et al. 2019) and is most likely an SGRB with extended emission (Sakamoto et al. 2016). This makes GRB 181123B one of a few SGRBs with a confirmed redshift at $z > 1.5$ and the highest-redshift secure SGRB to date with an optical afterglow detection.

We next examine the inferred afterglow and host galaxy properties of GRB 181123B in the context of the SGRB population. In Table 2, we present several properties for GRB 181123B, as well as where the event falls in the SGRB population as a percentile; in this scheme, a value of 50% is the median value of that parameter. At the most basic level, the faint apparent magnitude of the optical afterglow ($i \approx 25.1$ at ~ 9.1 hr) puts GRB 181123B in the lower 30%. However, when corrected for the redshift of the burst, GRB 181123B’s afterglow luminosity is slightly above the median of other SGRBs at similar rest-frame times.

The detection of both the X-ray and optical afterglows of GRB 181123B allows us to constrain the isotropic-equivalent kinetic energy scale and circumburst density to $E_{\text{K,iso}} \approx 1.3 \times 10^{51}$ erg and $n \approx 0.04$ – 1.1 cm^{-3} . For a direct comparison to GRB 111117A, we determine the allowed $E_{\text{K,iso}}-n$ parameter space in the same manner as described in Section 4 using the X-ray afterglow detection and optical upper limit (Margutti et al. 2012; Sakamoto et al. 2013) at $z = 2.211$, finding $E_{\text{K,iso}} = (1.4\text{--}2.3) \times 10^{51}$ erg and $n = 0.0045$ – 0.13 cm^{-3} , where the range is set by $\epsilon_B = 0.01$ – 0.1 . While the kinetic energy scales for both bursts are similar to those of SGRBs, with a median value of $\approx 2 \times 10^{51}$ erg (Fong et al. 2015), the inferred circumburst density of GRB 181123B is at the higher end of the population (Table 2). Recently, Wiggins et al. (2018) used cosmological simulations and population synthesis models for BNS mergers to predict the circum-merger densities as a function of redshift. Overall, they found that the fraction of mergers occurring in high-density environments increases with redshift, with the median density changing from $\approx 10^{-3} \text{ cm}^{-3}$ at $z < 0.5$ to $\approx 0.1 \text{ cm}^{-3}$ at $z > 1$. While the larger circumburst density of GRB 181123B seems to align with this predicted trend, we note that the other bursts with inferred densities of $> 0.1 \text{ cm}^{-3}$ predominantly originate at low redshifts of $z < 0.5$. Moreover, the expectation is for high circumburst densities to correspond to smaller offsets (modulo projection effects), but the projected physical offset of GRB 181123B is 5.08 ± 1.38 kpc, just below the population median of ≈ 6 kpc (W. Fong et al. 2020, in preparation). While the number of high-redshift bursts

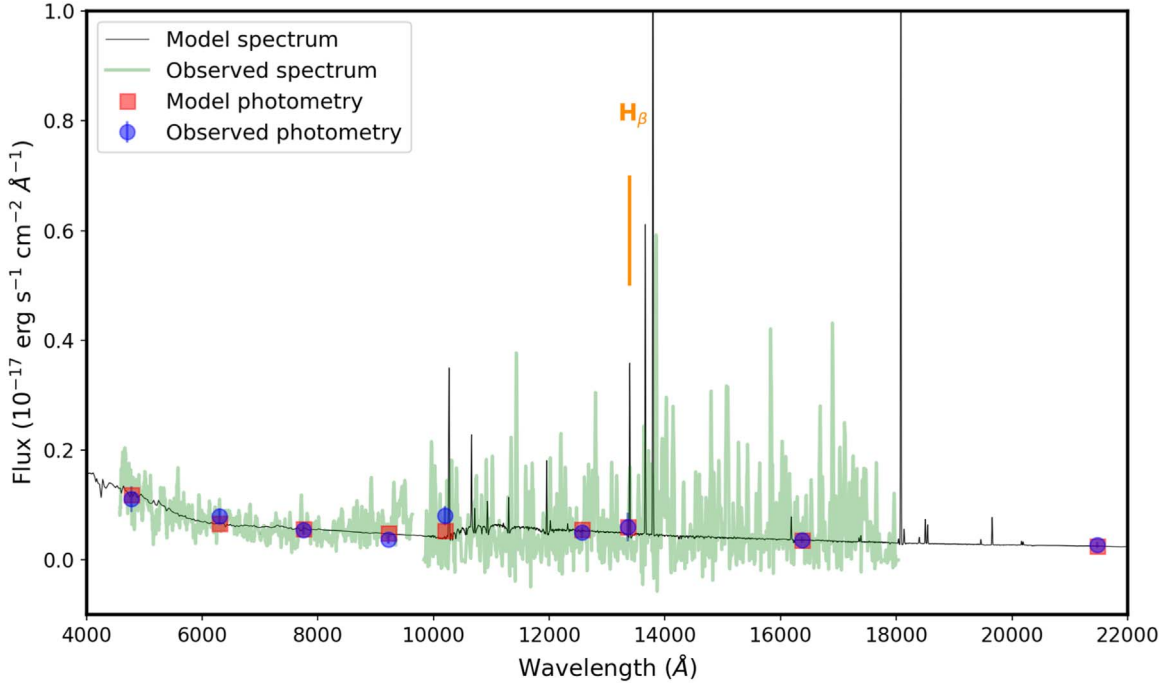


Figure 7. Photometry and spectrum of GRB 181123B’s host as a function of the observed wavelength, overplotted on the model spectrum and model photometry calculated from *Prospector* at $z = 1.754$. The orange line shows the position of the single emission line identified in the NIR spectrum. The model spectrum and photometry provide good agreement with the shape of the spectral continuum and the photometric colors.

Table 2
Comparison of Properties of GRB 181123B

| Properties | GRB 181123B | SGRBs ^a | GRB 111117A |
|------------------------------------|------------------------|--------------------|------------------|
| z | 1.754 ± 0.001 | 98% | 2.211 |
| T_{90} (s) | 0.26 ± 0.04 | 33% | 0.46 ± 0.05 |
| Hardness | 2.4 ± 0.6 | 78% | 2.8 ± 0.5 |
| $E_{\gamma, \text{iso}, 52}$ (erg) | 0.50 | 79% | 0.86 |
| $E_{K, \text{iso}, 52}^b$ (erg) | 0.13–0.14 | 39% | 0.14–0.23 |
| n^b (cm ⁻³) | 0.04–1.10 | 72%–95% | 0.005–0.13 |
| L (L^*) | 0.9 | 65% | 1.2 |
| $\log(M_*)$ (M_\odot) | $9.96^{+0.13}_{-0.16}$ | 51% | 9.9 |
| Age (Gyr) | $0.91^{+0.42}_{-0.45}$ | 44% | 0.5^c |
| Proj. offset (kpc) | 5.08 ± 1.38 | 44% | 10.52 ± 1.68 |

Notes. Values for GRB 111117A are taken from Lien et al. (2016) and Selsing et al. (2018), except for $E_{K, \text{iso}}$ and n , which are derived in this work. The SGRB comparison samples are from Fong et al. (2015, 2017) and Nugent et al. (2020).

^a Percentile for GRB 181123B compared to SGRB population.

^b Values assuming $\epsilon_B = 0.01$ –0.1.

^c This is the derived SSP age, so it can be taken as a lower limit on the true age of the stellar population (see Conroy 2013).

is admittedly too small at present for robust comparisons, based on the current sample at $z > 1.5$, we do not find any appreciable trends between SGRB afterglow properties and redshift.

To understand how GRB 181123B fits in the context of SGRB hosts, we collect data for 34 SGRBs with known redshifts and measured apparent r -band magnitudes of their host galaxies (m_r) from the literature (Leibler & Berger 2010; Levesque et al. 2010; Fong et al. 2013, 2017; Troja et al. 2016; Selsing et al. 2018, 2019; Lamb et al. 2019) and our own observations. We compare the values of m_r to the characteristic luminosity, L^* , across redshift using available galaxy

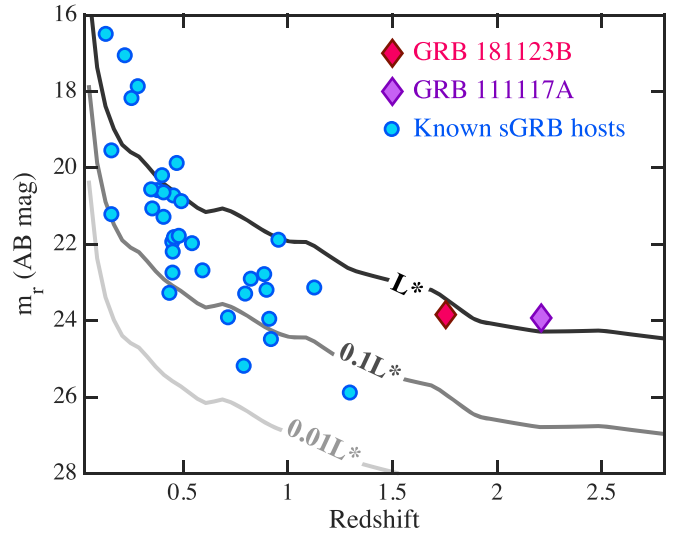


Figure 8. Host galaxy apparent r -band magnitude (m_r) of 34 SGRBs with known redshifts and optical measurements (blue circles). The high-redshift events GRB 181123B (this work) and GRB 111117A (Selsing et al. 2018) are highlighted as diamonds. Contours denote the evolving galaxy luminosity function across redshift corresponding to L^* , $0.1L^*$, and $0.01L^*$. Both GRB 181123B and GRB 111117A are $\sim L^*$ galaxies compared to those at contemporary redshifts (see text).

luminosity functions (Brown et al. 2001; Wolf et al. 2003; Willmer et al. 2006; Reddy & Steidel 2009; Finkelstein et al. 2015). For each redshift, we take the value of L^* in the band that corresponds to the observed r -band blueshifted to its rest frame at that redshift. We then interpolate across redshift to create smooth contours corresponding to L^* , $0.1L^*$, and $0.01L^*$. A comparison of the SGRB host population to the evolving galaxy luminosity function is shown in Figure 8. At $z \lesssim 1$, SGRB hosts span the luminosity range of ≈ 0.05 – $1L^*$, while at $z \gtrsim 1.5$, they are on the upper end of the luminosity function.

This trend can be easily explained by observational bias, as only the more luminous galaxies will be detectable at higher redshifts. At $L \approx 0.9L^*$, the host galaxy of GRB 181123B is similar to that of GRB 111117A ($1.2L^*$; Figure 8 and Selsing et al. 2018). In terms of stellar mass ($10^{9.96} M_\odot$) and (mass-weighted) stellar population age (0.9 Gyr), the host properties of GRB 181123B are also typical of the SGRB population, which has median values of $\approx 10^{9.96} M_\odot$ and 1.07 Gyr (Nugent et al. 2020; Table 2). The redshift and stellar population age of GRB 181123B imply that 50% of its stellar mass was formed when the universe was ≈ 2.8 Gyr old, corresponding to $z \sim 2.3$, around the peak of the cosmic SFR density (Madau & Dickinson 2014).

Next, we compare the host galaxy of GRB 181123B to the expected properties for galaxies at $z \approx 1.5$ –2. The rest-frame $U - V$ and $V - J$ colors have long been used to distinguish quiescent from SF galaxies to $z \sim 2$ (Williams et al. 2009). At $z = 1.754$, the rest-frame $U - V$ is roughly equivalent to $z - H$ or $Y - H$, which we calculate to be ≈ 1.2 and ≈ 1.1 mag, respectively, for GRB 181123B’s host galaxy. This places the host galaxy in the region occupied by unobscured SF galaxies in the UVJ diagram for all possible $V - J$ at $1.5 < z < 2.0$ (Fumagalli et al. 2014). Using the values of $\text{SFR} \approx 10 M_\odot \text{ yr}^{-1}$ and $\log(\text{sSFR}) \approx -8.9 \text{ yr}^{-1}$ derived from the SED, we find that the host of GRB 181123B lies just below the SF main sequence (SFMS) for galaxies of similar mass at the same redshift (Whitaker et al. 2014; Fang et al. 2018), and we find a similar result for the host of GRB 111117A based on the $H\alpha$ -derived SFR (Selsing et al. 2018).

6.2. SGRB Redshift Distribution and Implications for Delay Times

With the detection of GRB 181123B, there are only three Swift SGRBs with confirmed redshifts at $z > 1.5$ (and only seven SGRBs at $z > 1$). The apparent lack of SGRBs at high redshifts can be attributed to a combination of (i) Swift detector insensitivity at high redshifts (e.g., Guetta & Piran 2005; Behroozi et al. 2014), (ii) the difficulty of obtaining secure redshifts in the so-called “redshift desert” ($1.4 < z < 2.5$) in which all strong nebular emission lines are redshifted to $> 1 \mu\text{m}$ and $\text{Ly}\alpha$ is not yet accessible, and (iii) the intrinsic DTD, imprinted from an NS merger progenitor (Belczynski et al. 2006). In this section, we explore the constraints we can place from the observed SGRB redshift distribution on DTD models, with a focus on high- z ($z > 1.5$) events.

In the context of their binary merger progenitors, the true fraction of SGRBs that originate at $z > 1.5$ has implications for the merger timescale distribution, binary progenitor properties (e.g., initial separations, eccentricities; Selsing et al. 2019), and r -process element enrichment, which, in turn, can have effects on galaxy properties across redshift (O’Shaughnessy et al. 2010, 2017; Safarzadeh et al. 2019d; Simonetti et al. 2019). Of particular importance are the delay times, the time interval encompassing the stellar evolutionary and merger timescales, which impact our understanding of compact binary formation channels (isolated binary evolution versus dynamical assembly in globular clusters). The two main functional forms that have been widely considered in the literature are a power-law DTD (characterized by $t^{-\eta}$) and a lognormal DTD (characterized by mean delay time τ and width σ). The observed SGRB distribution peaks at $z \approx 0.5$ with a steep drop-off toward higher redshifts (Berger 2014; Fong et al. 2017), ostensibly

favoring a lognormal DTD with long delay times of several Gyr (Hao & Yuan 2013). This functional form could be explained by dynamical formation in globular clusters, in which the delay time strongly depends on the relaxation timescale of the cluster for NS binaries to assemble, which can be several Gyr (Spitzer 1987; Hopman et al. 2006; Kremer et al. 2019; Ye et al. 2019). On the other hand, a power-law DTD naturally arises for primordial binaries (i.e., systems that were born as a pair and have coevolved) given a power-law distribution of initial orbital separations and coalescence due to GW losses (Peters 1964; O’Shaughnessy et al. 2007; Dominik et al. 2012). Indeed, SN Ia studies have found that the observations are consistent with a DTD described by a power law with $\eta = 1$ (Totani et al. 2008; Maoz et al. 2012; Graur et al. 2014).

Thus far, studies of the Galactic BNS population (Vigna-Gómez et al. 2018), as well as SGRB host galaxy demographics, are in rough agreement with power-law DTDs with $\eta \gtrsim 1$ (Zheng & Ramirez-Ruiz 2007; Fong & Berger 2013). We note that some studies have found an excess of more rapid mergers, finding steeper DTDs than $\eta = 1$ (Beniamini & Piran 2019), but each provides fairly weak constraints. If we are indeed missing a population of high- z SGRBs, this would indicate overall shorter delay times and provide an additional constraint on the DTD. Some studies have also suggested a possible bimodal DTD distribution (Salvaterra et al. 2008), but this is in tension with more recent theoretical studies showing that dynamical assembly of NS–NS and NS–BH mergers can only contribute a small fraction to the overall merger rates (Belczynski et al. 2018; Ye et al. 2020).

The current observed SGRB redshift distribution comprises 43 events (updated from Fong et al. 2017) out of a total of 134 Swift SGRBs detected to date (Lien et al. 2016). This sample comprises all SGRBs with a secure host association ($P_{\text{cc}} < 0.1$), and a spectroscopic afterglow or host redshift, or a well-sampled photometric host redshift. This serves as an initial basis for comparison to predicted redshift distributions with varying underlying DTDs, star formation histories, and luminosity functions. Much work has been done in the literature to perform the convolution between these functions and predict the observed redshift distributions (Guetta & Piran 2005; Nakar et al. 2006; Hao & Yuan 2013; Wanderman & Piran 2015; Anand et al. 2018). From these works, we collect eight representative predicted distributions that cover the entire observed SGRB redshift range ($z \sim 0.1$ –2.5) and are not already ruled out by current observations. Four models describe lognormal DTDs with $\tau = 4$ and 6 Gyr and widths of $\sigma = 0.3$ and 1 Gyr (Nakar et al. 2006; Hao & Yuan 2013). The remaining four models are power-law DTDs with $\eta = 0.5$ –2 (Nakar et al. 2006; Jeong & Lee 2010; Hao & Yuan 2013). We note that models with the same DTD parameters (τ , σ , η) may give rise to slightly different distributions due to the underlying assumptions on the star formation histories, luminosity functions, and detector sensitivity, which can result in significant changes (Figure 9).

First, we use two-sample Kolmogorov–Smirnov (K-S) statistics to test the null hypothesis that each model is consistent with being drawn from the same underlying distribution as the observed redshift distribution of 43 SGRBs. With the exception of the lognormal distribution with $\tau = 4$ Gyr ($\sigma = 0.3$ Gyr) from Hao & Yuan (2013), which predicts a peak in the distribution at $z \approx 0.75$, all of the

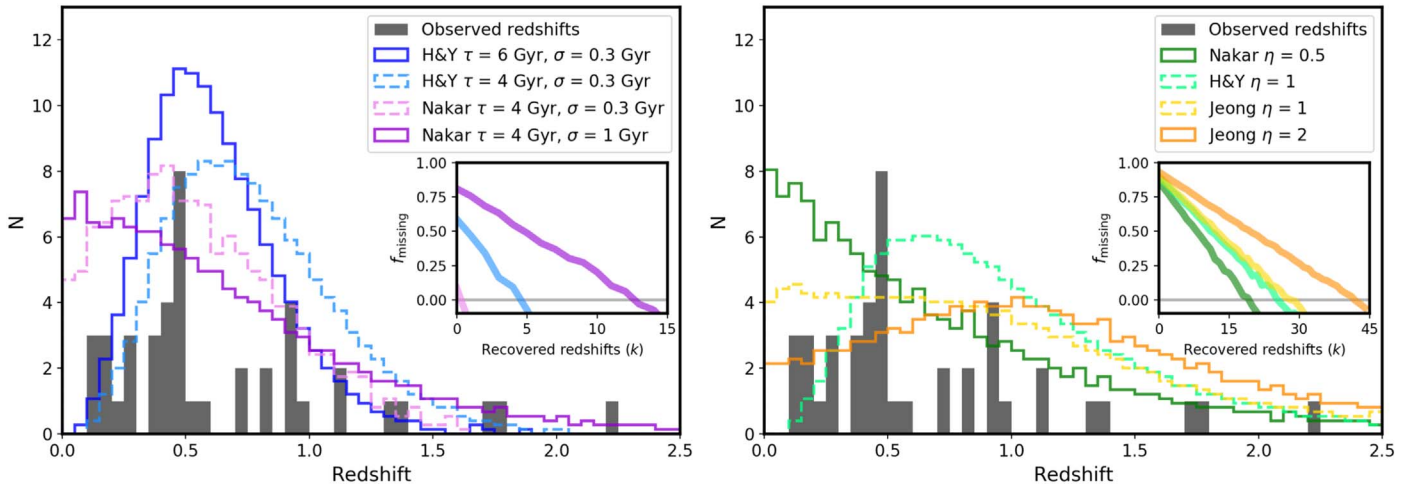


Figure 9. Redshift distribution of the 43 SGRBs with known redshifts (black histograms), plotted with the predicted observed redshift distributions derived from lognormal (left; Nakar et al. 2006; Hao & Yuan 2013) and power-law (right; Nakar et al. 2006; Jeong & Lee 2010; Hao & Yuan 2013) DTDs, representing the entire Swift SGRB population (134 events). The lognormal models favor lower redshifts, while the power-law models allow for more high- z bursts. The inset in each plot shows the 95% confidence upper limit on the missing fraction of high- z bursts ($z > 1.5$) as a function of the number of high- z bursts recovered (k) for each model. The gray horizontal line at a missing fraction of zero denotes the point when the respective model is ruled out to 95% confidence. As expected, the lognormal models that favor low redshifts are quickly ruled out with a few bursts recovered at high- z , while the power-law models can accommodate a larger number of high- z bursts.

lognormal distributions are consistent with being drawn from the same underlying distribution as the observed data, and we cannot reject the null hypothesis ($p = 0.45$ – 0.62). On the other hand, all of the power-law distributions with $\eta \geq 1$ result in $p < 0.05$ and thus are not consistent with being drawn from the same underlying distribution, while the power-law DTD characterized by $\eta = 0.5$ is consistent ($p = 0.3$). It is clear that without taking into account observational biases, distributions dominated by long delay times are preferred (Hao & Yuan 2013).

This analysis, however, neglects the inherent biases in the observed SGRB redshift distribution. Thus, we explore the fraction of Swift SGRBs that could be originating at high- z among the current population. Previous studies have found that $\approx 33\%$ – 70% of SGRBs could be missing at redshifts of $z > 0.7$ – 1 (Berger et al. 2007; Selsing et al. 2018). Over 2004–2020, Swift detected 134 SGRBs (including 13 with extended emission; Lien et al. 2016), and 43 have secure redshift determinations ($P_{\text{cc}} < 0.1$; 31%). In the large majority of cases, the determination of a redshift depends on an association with a host galaxy, which requires precise positional information from the detection of an X-ray or optical afterglow (\lesssim few arcsec precision). In the case of an afterglow detection, the lack of redshift can be attributed to the lack of a coincident host galaxy due to significant kicks and merger timescales, leaving large displacements between the burst and host galaxy (Berger 2010; Fong & Berger 2013; Tunnicliffe et al. 2014); offsets of $\gtrsim 10$ kpc are predicted to comprise as much as 40%–50% of the total population (Wiggins et al. 2018).²⁸ A faint host galaxy may also escape detection due to a low-luminosity or high- z origin (O’Connor et al. 2020). In this case, an apparently faint galaxy is more likely to originate at lower redshifts due to the increase in the faint-end slope of the galaxy luminosity function (Blanton et al. 2005; Parsa et al. 2016), although Figure 8 shows that SGRB hosts overall are drawn from the brighter end of the galaxy luminosity function. In total, the number of SGRBs that lack

redshift information is 91. If we assume that 50% of these events arise at $z > 1$, this translates to $\approx 34\%$ (46 events) of the current Swift SGRB population. If we take into account the 34 bursts that were subject to constraints that prevent the detection of an afterglow and subsequent redshift determination, such as satellite observing constraints, poor sight lines, or high Galactic extinction, and follow the same arguments as above, this results in $\approx 28\%$ (28 bursts) of the current population that was not subject to significant observing constraints. These numbers can be directly compared to expectations from DTDs.

We perform an exercise to explore how many SGRBs need to be recovered at high redshifts before a given model can be ruled out (“recovered redshifts”). We concentrate here on high redshifts given that these have comparatively greater discriminating power between DTD models than low-redshift events. To convert each of the eight continuous model distributions into a representative redshift distribution, we draw 1000 events from each model and then scale to 134 events (Figure 9). For each model, we determine the fraction of SGRBs that could originate at $z > 1.5$ as predicted by the model. To account for counting statistics, we draw 134 bursts from each model distribution 1000 times and determine the 95% confidence region on the high- z fraction. We then compute the missing fraction demanded by each model as a function of the number of additional recovered redshifts at $1.5 < z < 3$ (k), taking into account that there are already three known SGRBs at $z > 1.5$, so the observed population would be $3 + k$. In Figure 9, when the missing fraction goes to zero, the model can be ruled out to 95% confidence.

We find that lognormal models with small widths of $\sigma = 0.3$ Gyr can be ruled out for as few as $k \lesssim 1$ – 5 recovered redshifts, while the wider width, the $\sigma = 1$ Gyr model, could still accommodate $k = 13$ additional events recovered at $z > 1.5$. However, the shape of the low-redshift distribution is not supported by this model (Figure 9). For the power-law distributions, we find that a significantly larger number of high- z bursts are allowed before the models are ruled out to 95% confidence ($k \approx 19$ – 42 recovered redshifts), although models with $\eta = 0.5$ and 2 significantly under- or overpredict the

²⁸ We note that large kicks are at odds with those inferred from the Galactic BNS population; see Beniamini & Piran (2016) and Tauris et al. (2017).

$z < 1$ population. We find similar results if we perform the same analysis with a population of 100 events (representing the Swift SGRB population with no observing constraints). Performing a K-S test on each of the new distributions assuming 100 events shows agreement with the 134 event results. With the addition of high- z bursts to the observations, the data quickly favor the power-law distribution with $\eta = 1$, and all lognormal distributions are ruled out by the null hypothesis. Our analysis shows that the SGRB population is more consistent with power-law DTD models with $\eta = 1$, and the recovery of only a few high- z bursts, together with the shape of the low- z population, will help to solidify the model parameters. From the $\eta = 1$ power-law model, we find that the expected number of SGRBs that originate at $z > 1$ is ≈ 45 events (33% of the current population). Compared to our estimate that $\approx 34\%$ of Swift SGRBs originate at $z > 1$, this is another line of support for the $\eta = 1$ power-law model and thus a primordial NS binary formation channel.

In SNe Ia studies, similar work has been done to constrain the “prompt” fraction. Indeed, Rodney et al. (2014) found that observations suggest a prompt fraction of up to 50% (defined as events with delay times of < 500 Myr), with the results fully consistent with a power-law DTD with $\eta = 1$. For BNS mergers, most recent simulations require a prompt channel to explain r -process enrichment in Milky Way stars and ultrafaint dwarf galaxies (Matteucci et al. 2014; Beniamini et al. 2016a; Safarzadeh et al. 2019c; Simonetti et al. 2019). A reliable estimate of the prompt SGRB fraction would require a careful assessment of observational biases, the true SGRB redshift distribution, and stellar population ages as a proxy for the progenitor age distribution. Nevertheless, additional future detections of SGRBs at $z \approx 2$ and beyond might help to quantify the true prompt fraction of SGRBs.

7. Conclusions

We have presented the discovery of the optical afterglow and host galaxy of GRB 181123B at $z = 1.754$, contributing to a small but growing population of SGRBs at high redshifts. These results are based on a rapid-response and late-time follow-up campaign with Gemini, Keck, and the MMT. Our main conclusions are as follows.

1. After GRB 111117A ($z = 2.211$), GRB 181123B is the second most distant bona fide SGRB with a confirmed redshift measurement. It is the most distant SGRB to date with an optical afterglow detection.
2. The host galaxy of GRB 181123B is characterized by a stellar mass of $\approx 9.1 \times 10^9 M_\odot$, luminosity of $\approx 0.9 L^*$, and mass-weighted age of ≈ 0.9 Gyr. These are comparable to the median values of the SGRB host population across redshift.
3. Compared to the SFMS of galaxies at $1.5 < z < 2.0$, GRB 181123B lies just or significantly below this sequence and is thus forming stars at a lower rate than most SF galaxies of similar mass, indicating that it is moving toward quiescence.
4. The current redshift distribution comprises 43 events and is consistent with most lognormal distributions with moderate delay times (≈ 4 –6 Gyr). An analysis of the full Swift sample of 134 events, taking into account the difficulty of confirming high- z SGRBs, demonstrates that lognormal DTD models are overall disfavored. In

particular, models with moderate delay times of ≈ 4 –6 Gyr and small widths of $\sigma = 0.3$ Gyr can be ruled out to 95% confidence with an additional $\lesssim 1$ –5 Swift SGRBs recovered at $z > 1.5$. Lognormal models with wider widths of $\sigma = 1$ Gyr are less favored, given the lack of low- z SGRBs.

5. Power-law DTDs with an index around unity are more consistent with the data and can accommodate ≈ 30 recovered SGRBs at $z > 1.5$ (22% of the current population). For this model, ≈ 45 of the remaining SGRBs are expected to have $z > 1$ (33% of the current population). This is consistent with our estimates of the observed fraction of SGRBs originating at $z > 1$ of $\approx 34\%$ and with SGRBs originating from primordial NS binaries.

In order to properly constrain the DTD and probe the underlying formation channels of SGRBs and BNS mergers, it is important to uncover high- z bursts ($z > 1.5$). However, high- z bursts provide additional challenges for follow-up due to the additional observations needed and the resources available. The determination of the redshift of GRB 181123B required 6–10 m class telescopes and highlights the sheer difficulty of obtaining redshifts for host galaxies at $z > 1.5$, where the main spectral features are redshifted to NIR wavelengths with no major features at optical wavelengths. Moreover, even if SGRBs are drawn from the brighter end of the galaxy luminosity function, the host magnitudes are still $J \approx 22$ –23 mag. Dedicated efforts to characterize high- z candidates among the current population with state-of-the-art NIR instruments, as well as the planned James Webb Space Telescope and ELTs, will help to solidify the true high- z fraction among the current population. In the era of GW multimessenger astronomy, BNS mergers detected via GWs may also help constrain the DTD through studies of their host galaxies and connecting the redshift distributions of BNS mergers to those of SGRBs (e.g., Safarzadeh & Berger 2019; Safarzadeh et al. 2019b, 2019a).

We acknowledge Sarah Wellons, Allison Strom, and David Sand for helpful discussions that aided this work and Mansi Kasliwal for facilitating Keck observations. The Fong Group at Northwestern acknowledges support by the National Science Foundation under grant Nos. AST-1814782 and AST-1909358. This work was also supported in part by the National Aeronautics and Space Administration through grant HST-GO-15606.001-A from the Space Telescope Science Institute, which is operated by the Association of Universities for Research in Astronomy, Inc., under NASA contract NAS5-26555, and Chandra Award No. DD7-18095X, issued by the Chandra X-ray Center, which is operated by the Smithsonian Astrophysical Observatory for and on behalf of NASA under contract NAS8-03060. M.N. is supported by a Royal Astronomical Society Research Fellowship. A.J.L. has received funding from the European Research Council (ERC) under the European Union’s Horizon 2020 research and innovation program (grant agreement No. 725246, TEDE; PI: Levan). A. A.M. is funded by the Large Synoptic Survey Telescope Corporation, the Brinson Foundation, and the Moore Foundation in support of the LSSTC Data Science Fellowship Program; he also receives support as a CIERA Fellow from the CIERA Postdoctoral Fellowship Program (Center for Interdisciplinary Exploration and Research in Astrophysics,

Northwestern University). J.L. is supported by an NSF Astronomy and Astrophysics Postdoctoral Fellowship under award AST-1701487. K.D.A. acknowledges support provided by NASA through the NASA Hubble Fellowship grant HST-HF2-51403.001-A awarded by the Space Telescope Science Institute, which is operated by the Association of Universities for Research in Astronomy, Inc., for NASA, under contract NAS5-26555.

Based on observations obtained at the international Gemini Observatory (PIs: Paterson, Fong; Program IDs GS-2018B-Q-112, GN-2018B-Q-117, GS-2019A-FT-107), a program of NOIRLab, which is managed by the Association of Universities for Research in Astronomy (AURA) under a cooperative agreement with the National Science Foundation on behalf of the Gemini Observatory partnership: the National Science Foundation (United States), National Research Council (Canada), Agencia Nacional de Investigación y Desarrollo (Chile), Ministerio de Ciencia, Tecnología e Innovación (Argentina), Ministério da Ciência, Tecnologia, Inovações e Comunicações (Brazil), and Korea Astronomy and Space Science Institute (Republic of Korea).


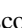
W. M. Keck Observatory and MMT Observatory access was supported by Northwestern University and the Center for Interdisciplinary Exploration and Research in Astrophysics (CIERA). Some of the data presented herein were obtained at the W. M. Keck Observatory (PIs: Miller, Fong, Paterson; Programs 2018B_NW254, 2018B_NW249, 2019A_O329), which is operated as a scientific partnership among the California Institute of Technology, the University of California, and the National Aeronautics and Space Administration. The Observatory was made possible by the generous financial support of the W. M. Keck Foundation. The authors wish to recognize and acknowledge the very significant cultural role and reverence that the summit of Maunakea has always had within the indigenous Hawaiian community. We are most fortunate to have the opportunity to conduct observations from this mountain. Observations reported here were obtained at the MMT Observatory, a joint facility of the University of Arizona and the Smithsonian Institution (PI: Fong; Programs 2018C-UAO-G4, 2019A-UAO-G7, 2020A-UAO-G212-20A).














This research was supported in part through the computational resources and staff contributions provided for the Quest high-performance computing facility at Northwestern University, which is jointly supported by the Office of the Provost, the Office for Research, and Northwestern University Information Technology.

This work made use of data supplied by the UK Swift Science Data Centre at the University of Leicester.

Facilities: Swift (XRT and UVOT), Gemini-North (GMOS), Gemini-South (GMOS, FLAMINGOS-2), Keck:I (MOSFIRE), Keck:II (DEIMOS), MMT (MMIRS).

ORCID iDs

K. Paterson  <https://orcid.org/0000-0001-8340-3486>
 W. Fong  <https://orcid.org/0000-0002-7374-935X>
 A. Nugent  <https://orcid.org/0000-0002-2028-9329>
 A. Rouco Escorial  <https://orcid.org/0000-0003-3937-0618>
 J. Leja  <https://orcid.org/0000-0001-6755-1315>
 T. Laskar  <https://orcid.org/0000-0003-1792-2338>
 R. Chornock  <https://orcid.org/0000-0002-7706-5668>
 A. A. Miller  <https://orcid.org/0000-0001-9515-478X>
 J. Scharwächter  <https://orcid.org/0000-0003-1585-9486>

S. B. Cenko  <https://orcid.org/0000-0003-1673-970X>
 D. Perley  <https://orcid.org/0000-0001-8472-1996>
 N. R. Tanvir  <https://orcid.org/0000-0003-3274-6336>
 A. Levan  <https://orcid.org/0000-0001-7821-9369>
 A. Cucchiara  <https://orcid.org/0000-0001-6455-5660>
 B. E. Cobb  <https://orcid.org/0000-0002-9118-9448>
 K. De  <https://orcid.org/0000-0002-8989-0542>
 E. Berger  <https://orcid.org/0000-0002-9392-9681>
 G. Terreran  <https://orcid.org/0000-0003-0794-5982>
 K. D. Alexander  <https://orcid.org/0000-0002-8297-2473>
 M. Nicholl  <https://orcid.org/0000-0002-2555-3192>
 P. K. Blanchard  <https://orcid.org/0000-0003-0526-2248>
 D. Cornish  <https://orcid.org/0000-0002-1533-9037>

References

- Abbott, B. P., Abbott, R., Abbott, T. D., et al. 2017a, *PhRvL*, **119**, 161101
 Abbott, B. P., Abbott, R., Abbott, T. D., et al. 2017b, *ApJL*, **848**, L13
 Abbott, B. P., Abbott, R., Abbott, T. D., et al. 2020, *ApJL*, **892**, L3
 Ahn, C. P., Alexandroff, R., Allende Prieto, C., et al. 2012, *ApJS*, **203**, 21
 Anand, N., Shahid, M., & Resmi, L. 2018, *MNRAS*, **481**, 4332
 Anderson, G. E., Bell, M. E., Stevens, J., et al. 2018, *GCN*, 23467, 1
 Antonelli, L. A., D’Avanzo, P., Perna, R., et al. 2009, *A&A*, **507**, L45
 Arnaud, K. A. 1996, in *ASP Conf. Ser. 101*, XSPEC: The First Ten Years, ed. G. H. Jacoby & J. Barnes (San Francisco, CA: ASP), 17
 Astropy Collaboration, Robitaille, T. P., Tollerud, E. J., et al. 2013, *A&A*, **558**, A33
 Barthelmy, S. D., Barbier, L. M., Cummings, J. R., et al. 2005, *SSRv*, **120**, 143
 Becker, A. 2015, HOTPANTS: High Order Transform of PSF ANd Template Subtraction v5.1.11, Astrophysics Source Code Library, ascl:1504.004
 Behroozi, P. S., Ramirez-Ruiz, E., & Fryer, C. L. 2014, *ApJ*, **792**, 123
 Belczynski, K., Askar, A., Arca-Sedda, M., et al. 2018, *A&A*, **615**, A91
 Belczynski, K., Perna, R., Bulik, T., et al. 2006, *ApJ*, **648**, 1110
 Beniamini, P., Hotokezaka, K., & Piran, T. 2016a, *ApJL*, **829**, L13
 Beniamini, P., Nava, L., & Piran, T. 2016b, *MNRAS*, **461**, 51
 Beniamini, P., & Piran, T. 2016, *MNRAS*, **456**, 4089
 Beniamini, P., & Piran, T. 2019, *MNRAS*, **487**, 4847
 Bennett, C. L., Larson, D., Weiland, J. L., & Hinshaw, G. 2014, *ApJ*, **794**, 135
 Berger, E. 2009, *ApJ*, **690**, 231
 Berger, E. 2010, *ApJ*, **722**, 1946
 Berger, E. 2014, *ARA&A*, **52**, 43
 Berger, E., Fox, D. B., Price, P. A., et al. 2007, *ApJ*, **664**, 1000
 Berger, E., Zauderer, B. A., Levan, A., et al. 2013, *ApJ*, **765**, 121
 Blanton, M. R., Lupton, R. H., Schlegel, D. J., et al. 2005, *ApJ*, **631**, 208
 Bloom, J. S., Kulkarni, S. R., & Djorgovski, S. G. 2002, *AJ*, **123**, 1111
 Brown, W. R., Geller, M. J., Fabricant, D. G., & Kurtz, M. J. 2001, *AJ*, **122**, 714
 Calzetti, D., Armus, L., Bohlin, R. C., et al. 2000, *ApJ*, **533**, 682
 Cardelli, J. A., Clayton, G. C., & Mathis, J. S. 1989, *ApJ*, **345**, 245
 Chabrier, G. 2003, *PASP*, **115**, 763
 Champion, D. J., Lorimer, D. R., McLaughlin, M. A., et al. 2004, *MNRAS*, **350**, L61
 Church, R. P., Levan, A. J., Davies, M. B., & Tanvir, N. 2011, *MNRAS*, **413**, 2004
 Collins, K. A., Kielkopf, J. F., Stassun, K. G., & Hessman, F. V. 2017, *AJ*, **153**, 77
 Conroy, C. 2013, *ARA&A*, **51**, 393
 Conroy, C., & Gunn, J. E. 2010, FSPS: Flexible Stellar Population Synthesis, Astrophysics Source Code Library, ascl:1010.043
 Conroy, C., Gunn, J. E., & White, M. 2009, *ApJ*, **699**, 486
 Craig, M., Crawford, S., Seifert, M., et al. 2017, *astropy/ccdproc*: v1.3.0.post1, Zenodo, doi:10.5281/zenodo.1069648
 Crampton, D., Fletcher, J. M., Jean, I., et al. 2000, *Proc. SPIE*, **4008**, 114
 Cushing, M. C., Vacca, W. D., & Rayner, J. T. 2004, *PASP*, **116**, 362
 de Jager, O. C., & Harding, A. K. 1992, *ApJ*, **396**, 161
 Dominik, M., Belczynski, K., Fryer, C., et al. 2012, *ApJ*, **759**, 52
 Eikenberry, S. S., Elston, R., Raines, S. N., et al. 2004, *Proc. SPIE*, **5492**, 1196
 Eisenstein, D. J., Weinberg, D. H., Agol, E., et al. 2011, *AJ*, **142**, 72
 Evans, P. A., Beardmore, A. P., Page, K. L., et al. 2009, *MNRAS*, **397**, 1177
 Faber, S. M., Phillips, A. C., Kibrick, R. I., et al. 2003, *Proc. SPIE*, **4841**, 1657
 Fang, J. J., Faber, S. M., Koo, D. C., et al. 2018, *ApJ*, **858**, 100
 Finkelstein, S. L., Ryan, R. E. J., Papovich, C., et al. 2015, *ApJ*, **810**, 71
 Fong, W., & Berger, E. 2013, *ApJ*, **776**, 18

- Fong, W., Berger, E., Blanchard, P. K., et al. 2017, *ApJL*, **848**, L23
- Fong, W., Berger, E., Chornock, R., et al. 2013, *ApJ*, **769**, 56
- Fong, W., Berger, E., & Fox, D. B. 2010, *ApJ*, **708**, 9
- Fong, W., Berger, E., Margutti, R., & Zauderer, B. A. 2015, *ApJ*, **815**, 102
- Fong, W., Tanvir, N. R., & Levan, A. J. 2018, GCN, **23439**, 1
- Fox, D. B., Frail, D. A., Price, P. A., et al. 2005, *Natur*, **437**, 845
- Frater, R. H., Brooks, J. W., & Whiteoak, J. B. 1992, *JEEEA*, **12**, 103
- Fukugita, M., Ichikawa, T., Gunn, J. E., et al. 1996, *AJ*, **111**, 1748
- Fumagalli, M., Labbé, I., Patel, S. G., et al. 2014, *ApJ*, **796**, 35
- Gaia Collaboration, Brown, A. G. A., Vallenari, A., et al. 2018, *A&A*, **616**, A1
- Gaia Collaboration, Prusti, T., de Bruijne, J. H. J., et al. 2016, *A&A*, **595**, A1
- Gehrels, N., Chincarini, G., Giommi, P., et al. 2004, *ApJ*, **611**, 1005
- Goad, M. R., Tyler, L. G., Beardmore, A. P., et al. 2007, *A&A*, **476**, 1401
- Goldstein, A., Veres, P., Burns, E., et al. 2017, *ApJL*, **848**, L14
- Gompertz, B. P., Levan, A. J., Tanvir, N. R., et al. 2018, *ApJ*, **860**, 62
- Granot, J., & Sari, R. 2002, *ApJ*, **568**, 820
- Graur, O., Rodney, S. A., Maoz, D., et al. 2014, *ApJ*, **783**, 28
- Guetta, D., & Piran, T. 2005, *A&A*, **435**, 421
- Gunn, J. E., Siegmund, W. A., Mannery, E. J., et al. 2006, *AJ*, **131**, 2332
- Hajela, A., Margutti, R., Alexander, K. D., et al. 2019, *ApJL*, **886**, L17
- Hao, J.-M., & Yuan, Y.-F. 2013, *A&A*, **558**, A22
- Hewett, P. C., Warren, S. J., Leggett, S. K., & Hodgkin, S. T. 2006, *MNRAS*, **367**, 454
- Hjorth, J., Sollerman, J., Gorosabel, J., et al. 2005a, *ApJL*, **630**, L117
- Hjorth, J., Watson, D., Fynbo, J. P. U., et al. 2005b, *Natur*, **437**, 859
- Hodgkin, S. T., Irwin, M. J., Hewett, P. C., & Warren, S. J. 2009, *MNRAS*, **394**, 675
- Hopman, C., Guetta, D., Waxman, E., & Portegies Zwart, S. 2006, *ApJL*, **643**, L91
- Hotokezaka, K., Beniamini, P., & Piran, T. 2018, *IJMPD*, **27**, 1842005
- Jeong, S., & Lee, C.-H. 2010, *JKPS*, **56**, 1619
- Johnson, B., & Leja, J. 2017, bd-j/prospector: Initial release, vv0.1, Zenodo, doi:10.5281/zenodo.1116491
- Kennicutt, R. C. J. 1998, *ApJ*, **498**, 541
- Kocevski, D., Thöne, C. C., Ramirez-Ruiz, E., et al. 2010, *MNRAS*, **404**, 963
- Kremer, K., Chatterjee, S., Ye, C. S., Rodriguez, C. L., & Rasio, F. A. 2019, *ApJ*, **871**, 38
- Lamb, G. P., Tanvir, N. R., Levan, A. J., et al. 2019, *ApJ*, **883**, 48
- Lawrence, A., Warren, S. J., Almaini, O., et al. 2007, *MNRAS*, **379**, 1599
- Leibler, C. N., & Berger, E. 2010, *ApJ*, **725**, 1202
- Leja, J., Johnson, B. D., Conroy, C., van Dokkum, P. G., & Byler, N. 2017, *ApJ*, **837**, 170
- Levesque, E. M., Bloom, J. S., Butler, N. R., et al. 2010, *MNRAS*, **401**, 963
- Lien, A., Sakamoto, T., Barthelmy, S. D., et al. 2016, *ApJ*, **829**, 7
- Lien, A. Y., D'Avanzo, P., & Palmer, D. M. 2018, GCN, **23432**, 1
- Lindgren, L., Hernández, J., Bombrun, A., et al. 2018, *A&A*, **616**, A2
- Lipunov, V., Gorbvskoy, E., Kornilov, V., et al. 2018, GCN, **23444**, 1
- Lipunov, V., Kornilov, V., Gorbvskoy, E., et al. 2010, *AdAst*, **2010**, 349171
- Madau, P., & Dickinson, M. 2014, *ARA&A*, **52**, 415
- Maoz, D., Mannucci, F., & Brandt, T. D. 2012, *MNRAS*, **426**, 3282
- Margutti, R., Berger, E., Fong, W., et al. 2012, *ApJ*, **756**, 63
- Matteucci, F., Romano, D., Arcones, A., Korobkin, O., & Rosswog, S. 2014, *MNRAS*, **438**, 2177
- McLean, I. S., Steidel, C. C., Epps, H. W., et al. 2012, *Proc. SPIE*, **8446**, 84460J
- McLeod, B., Fabricant, D., Nystrom, G., et al. 2012, *PASP*, **124**, 1318
- Metzger, B. D. 2017, *LRR*, **20**, 3
- Moustakas, J., Kennicutt, R. C. J., & Tremonti, C. A. 2006, *ApJ*, **642**, 775
- Nakar, E., Ando, S., & Sari, R. 2009, *ApJ*, **703**, 675
- Nakar, E., Gal-Yam, A., & Fox, D. B. 2006, *ApJ*, **650**, 281
- Norris, J. P., Barthelmy, S. D., & Lien, A. Y. 2018, GCN, **23443**, 1
- Nugent, A. E., Fong, W., & Dong, Y. 2020, arXiv:2007.10372
- O'Connor, B., Beniamini, P., & Kouveliotou, C. 2020, *MNRAS*, **495**, 4782
- O'Shaughnessy, R., Bellovary, J. M., Brooks, A., et al. 2017, *MNRAS*, **464**, 2831
- O'Shaughnessy, R., Kalogera, V., & Belczynski, K. 2010, *ApJ*, **716**, 615
- O'Shaughnessy, R., Kopparapu, R., & Hanna, C. 2007, AAS Meeting, **211**, 49.01
- Oates, S. R., & Lien, A. Y. 2018, GCN, **23437**, 1
- Osborne, J. P., Beardmore, A. P., Evans, P. A., & Goad, M. R. 2018, GCN, **23434**, 1
- Parsa, S., Dunlop, J. S., McLure, R. J., & Mortlock, A. 2016, *MNRAS*, **456**, 3194
- Paterson, K., & Fong, W. 2018, GCN, **23440**, 1
- Paterson, K., Fong, W., de, K., et al. 2018, GCN, **23461**, 1
- Peters, P. C. 1964, *PhRv*, **136**, 1224
- Postnov, K. A., & Yungelson, L. R. 2014, *LRR*, **17**, 3
- Price, S. H., Kriek, M., Brammer, G. B., et al. 2014, *ApJ*, **788**, 86
- Price-Whelan, A. M., Sipőcz, B. M., Günther, H. M., et al. 2018, *AJ*, **156**, 123
- Reddy, N. A., & Steidel, C. C. 2009, *ApJ*, **692**, 778
- Rodney, S. A., Riess, A. G., Strolger, L.-G., et al. 2014, *AJ*, **148**, 13
- Safarzadeh, M., & Berger, E. 2019, *ApJL*, **878**, L12
- Safarzadeh, M., Berger, E., Leja, J., & Speagle, J. S. 2019a, *ApJL*, **878**, L14
- Safarzadeh, M., Berger, E., Ng, K. K. Y., et al. 2019b, *ApJL*, **878**, L13
- Safarzadeh, M., Ramirez-Ruiz, E., Andrews, J. J., et al. 2019c, *ApJ*, **872**, 105
- Safarzadeh, M., Sarmento, R., & Scannapieco, E. 2019d, *ApJ*, **876**, 28
- Sakamoto, T., Barthelmy, S. D., Cummings, J. R., et al. 2016, GCN, **19276**, 1
- Sakamoto, T., Troja, E., Aoki, K., et al. 2013, *ApJ*, **766**, 41
- Salvaterra, R., Cerutti, A., Chincarini, G., et al. 2008, *MNRAS*, **388**, L6
- Santana, R., Barniol Duran, R., & Kumar, P. 2014, *ApJ*, **785**, 29
- Sari, R., & Esin, A. A. 2001, *ApJ*, **548**, 787
- Sari, R., Piran, T., & Narayan, R. 1998, *ApJL*, **497**, L17
- Savchenko, V., Ferrigno, C., Kuulkers, E., et al. 2017, *ApJL*, **848**, L15
- Savitzky, A., & Golay, M. J. E. 1964, *Anal. Chem.*, **36**, 1627
- Schlaflly, E. F., & Finkbeiner, D. P. 2011, *ApJ*, **737**, 103
- Selsing, J., Krühler, T., Malesani, D., et al. 2018, *A&A*, **616**, A48
- Selsing, J., Malesani, D., Goldoni, P., et al. 2019, *A&A*, **623**, A92
- Selsing, J., Vreeswijk, P. M., Japel, J., et al. 2016, GCN, **19274**, 1
- Simonetti, P., Matteucci, F., Greggio, L., & Cescutti, G. 2019, *MNRAS*, **486**, 2896
- Skilling, J. 2004, in AIP Conf. Ser. 735, Bayesian Inference and Maximum Entropy Methods in Science and Engineering, ed. R. Fischer, R. Preuss, & U. V. Toussaint (Melville, NY: AIP), **395**
- Skilling, J. 2006, *BayAn*, **1**, 833
- Skrutskie, M. F., Cutri, R. M., Stiening, R., et al. 2006, *AJ*, **131**, 1163
- Soderberg, A. M., Berger, E., Kasliwal, M., et al. 2006, *ApJ*, **650**, 261
- Speagle, J. S. 2020, *MNRAS*, **493**, 3132
- Spitzer, L. 1987, Dynamical Evolution of Globular Clusters (Princeton, NJ: Princeton Univ. Press)
- Tanaka, M. 2016, *AdAst*, **2016**, 634197
- Tanvir, N. R., Levan, A. J., Fruchter, A. S., et al. 2013, *Natur*, **500**, 547
- Tauris, T. M., Kramer, M., Freire, P. C. C., et al. 2017, *ApJ*, **846**, 170
- Tody, D. 1986, *Proc. SPIE*, **627**, 733
- Totani, T., Morokuma, T., Oda, T., Doi, M., & Yasuda, N. 2008, *PASJ*, **60**, 1327
- Troja, E., Castro-Tirado, A. J., Becerra González, J., et al. 2019, *MNRAS*, **489**, 2104
- Troja, E., Sakamoto, T., Cenko, S. B., et al. 2016, *ApJ*, **827**, 102
- Tunnicliffe, R. L., Levan, A. J., Tanvir, N. R., et al. 2014, *MNRAS*, **437**, 1495
- Vacca, W. D., Cushing, M. C., & Rayner, J. T. 2003, *PASP*, **115**, 389
- Vigna-Gómez, A., Neijssel, C. J., Stevenson, S., et al. 2018, *MNRAS*, **481**, 4009
- Wanderman, D., & Piran, T. 2015, *MNRAS*, **448**, 3026
- Whitaker, K. E., Franx, M., Leja, J., et al. 2014, *ApJ*, **795**, 104
- Wiggins, B. K., Fryer, C. L., Smidt, J. M., et al. 2018, *ApJ*, **865**, 27
- Williams, R. J., Quadri, R. F., Franx, M., van Dokkum, P., & Labbé, I. 2009, *ApJ*, **691**, 1879
- Willingale, R., Starling, R. L. C., Beardmore, A. P., Tanvir, N. R., & O'Brien, P. T. 2013, *MNRAS*, **431**, 394
- Willmer, C. N. A., Faber, S. M., Koo, D. C., et al. 2006, *ApJ*, **647**, 853
- Wolf, C., Meisenheimer, K., Rix, H. W., et al. 2003, *A&A*, **401**, 73
- Wu, Y., & MacFadyen, A. 2018, *ApJ*, **869**, 55
- Ye, C. S., Fong, W.-f., Kremer, K., et al. 2020, *ApJL*, **888**, L10
- Ye, C. S., Kremer, K., Chatterjee, S., Rodriguez, C. L., & Rasio, F. A. 2019, *ApJ*, **877**, 122
- Zhang, B.-B., van Eerten, H., Burrows, D. N., et al. 2015, *ApJ*, **806**, 15
- Zheng, Z., & Ramirez-Ruiz, E. 2007, *ApJ*, **665**, 1220